日本磁気学会
ISSN 2432-0250
Journal of the Magnetics Society of Japan
Electronic Journal URL: https://www.jstage.jst.go.jp/browse/msjmag

Vol.44 No.2　2020

Journal

JOURNAL OF THE MAGNETICS SOCIETY OF JAPAN

Vol.44 No.2 2020

日本磁気学会

ISSN 2432-0250

HP: http://www.magnetics.jp/ e-mail: msj@bj.wakwak.com

Electronic Journal: http://www.jstage.jst.go.jp/browse/msjmag

米国Veeco社製イオンソース

SOLUS DC Ion Source Controllers

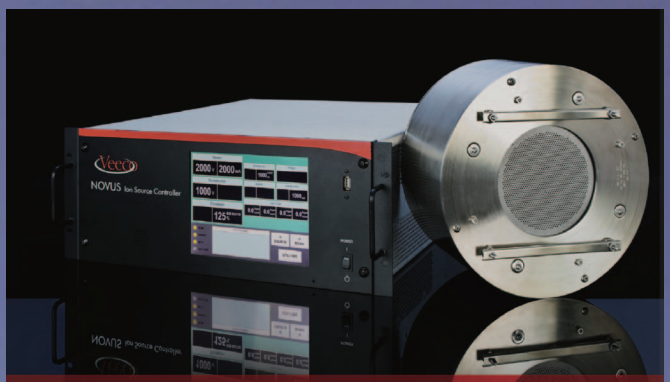

NOVUS RF Ion Source Power Supply

米国Veeco社は業界唯一のリニアグリッドソースなど幅広い用途に対応するイオンソースを持つ世界有数の薄膜プロセス装置メーカーであり、イオンソースのNo.1メーカーです。
ラインナップも小型3cm～リニア1.1mタイプまでRF用/DC用と幅広く取り揃えており、
世界中から高評価を得ている高品質で高機能なイオンソースです。

受託クリーニング加工

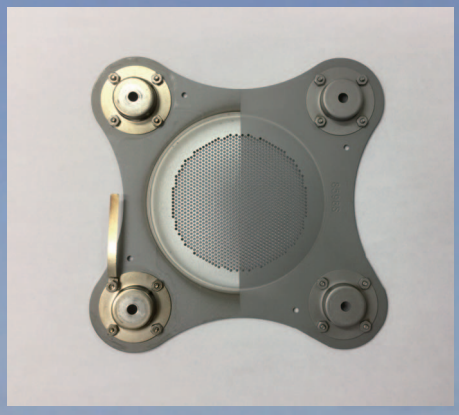

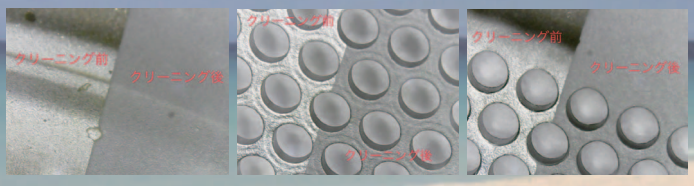

溶剤を使用せず商材へのダメージを極力抑える手法により、形状変化が原因で使用不可となる精密部品などのクリーニングに対応しております。
その他、IBS等の強固な膜にも対応しております。

キヤノンオプトロン社製蒸着材料

幅広い分野で活用されている薄膜技術の源となる蒸着材料において、キヤノンオプトロン社は多種多様なニーズに対応でき高品質で安定供給が可能な国内No.1メーカーです。

OSI
株式会社 オーエスアイ
〒103-0014 東京都中央区日本橋蛎殻町2-5-4-704
TEL：03-6861-7028　FAX：03-6700-6930
http://www.osi-opt.com
E-mail：info@osi-opt.com

世界初！
高温超電導型VSM

新製品

世界初*、高温超電導マグネットをVSMに採用することで
測定速度 当社従来機1/20を実現。
0.5mm cube磁石のBr, HcJ高精度測定が可能と
なりました。
*2014年7月 東英工業調べ

測定結果例

高温超電導VSMによるNdFeB(sint.) 0.5mm cube BHカーブ

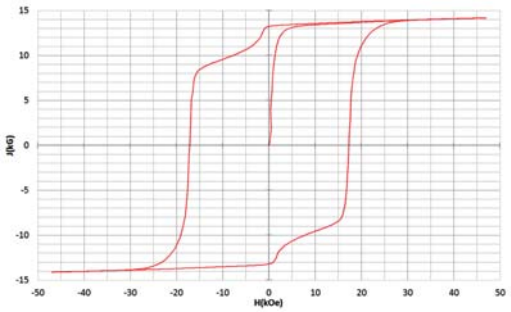

磁化測定レンジ：0.2emu
Br = 13.2kG　　HcJ = 17.2kOe

高温超電導VSMによるNdFeB(sint.) 1mm cube BHカーブ

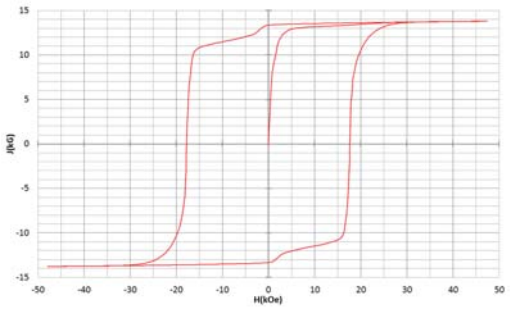

磁化測定レンジ：2emu
Br = 13.3kG　　HcJ = 17.7kOe

高温超電導VSMによるNdFeB(sint.) 4mm cube BHカーブ

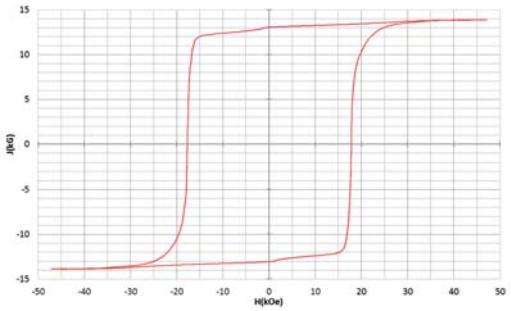

磁化測定レンジ：100emu
Br = 13.1kG　　HcJ = 17.8kOe

高速測定を実現

高温超電導マグネット採用により、高速測定を実現しました。Hmax= 5Tesla, Full Loop 測定が2分で可能です。
（当社従来機：Full Loop測定　40分）

小試料のBr,HcJ高精度測定

0.5mm cube 磁石のBr,HcJ高精度測定ができ、表面改質領域を切り出しBr,HcJの強度分布等、微小変化量の比較測定が可能です。
また、試料の加工劣化の比較測定が可能です。

試料温度可変測定

−50℃～+200℃温度可変UNIT（オプション）

磁界発生部の小型化

マグネットシステム部寸法：0.8m×0.3m×0.3m

TOEI 東英工業株式会社
http://www.toeikogyo.co.jp
〒194-0035 東京都町田市忠生1-8-13
TEL：042-791-1211　FAX：042-792-0490
E-mail : sales@toeikogyo.co.jp

Journal of the Magnetics Society of Japan
Vol. 44, No. 2

Electronic Journal URL: https://www.jstage.jst.go.jp/browse/msjmag

CONTENTS

J. Magn. Soc. Jpn., **44**, 26-29 (2020)

Letter

Estimation of Rectifying Performance for Terahertz Wave in Newly Designed Fe/ZnO/MgO/Fe Magnetic Tunnel Junction

H. Saito, and H. Imamura

National Institute of Advanced Industrial Science and Technology (AIST) Spintronics Research Center, Central 2, 1-1-1 Umezono, Tsukuba 305-8568, Japan

We fabricated fully epitaxial Fe/ZnO/MgO/Fe magnetic tunnel junctions (MTJs) with low junction resistance-area products (several Ωμm^2) and conducted a theoretical estimation of square-low rectifying performance for a terahertz electromagnetic wave. Effective current responsivity up to 0.09 A/W at 1 THz was obtained under zero-bias voltage condition at room temperature. The result is approximately half the value of the best result obtained for experiments in semiconductor-based diodes, performed under similar conditions. The study strongly suggests that this MTJ system has a great potential for the rectifying element of the terahertz wave.

Key words: magnetic tunnel junction, epitaxial, high-frequency, terahertz, rectification,

1. Introduction

Studies concerning terahertz (THz) wave, having a frequency (f) range from 100 GHz to 10 THz, have recently emerged in expectation with the great potentials for novel applications such as ultra-fast wireless communications[1-3] and non-destructive imaging.[4,5] A THz wave receiver is one of the crucial building blocks of such THz applications[6]. However, developments of high-performance THz devices including the receiver are still challenging issues because using the corresponding frequencies leaves a "gap" between those for conventional electronics and optics system. Low manufacturing cost is also an important requirement from a practical device point of view.

Metal-insulator-metal (MIM) tunnel diodes are attractive rectifying element for the THz/far infrared applications[7-14] in this respect. Although the MIM diode has been generally considered as possessing poor rectifying performance when compared with semiconductor-based diodes, it has the advantage of realizing very low junction resistance-area products (R_DA) of below 1 Ωμm^2 at a zero-bias voltage. This leads to the shorter RC time constant, and thereby resulting in higher cut-off frequency of the system, compared to the semiconductor-based diodes. Moreover, the MIM diode is suitable for mass-production due to its feasibility of employing conventional manufacturing growth methods, such as a sputtering, even on a flexible substrate[15] at low temperatures.

Very recently, we found a strong diodic behavior in the current-voltage (I–V) characteristics in epitaxial MI(I)M device of Fe(001)/ZnO(001)/MgO(001)/Fe(001) magnetic tunnel junction (MTJs) at room temperature (RT)[16], in which tunneling magnetoresistance (TMR) is caused by so called spin-polazied coherent tunneling[17,18]. We theoretically estimated the effective current responsivity (β_{eff}) of the MTJ system, which correnponds to the conversion capability from a high-frequency to a DC current, in regards to the ZnO and MgO barrier thicknesses (t_{ZnO} and t_{MgO}, respectively) as well as the junction area (A)[19]. The calculation predicted that β_{eff} can reach up to 0.12 A/W at 1 THz with the conditions, $t_{ZnO} \sim t_{MgO}$ with low R_DA (a few Ωμm^2) and small A (~ 0.01 μm^2). The obtained β_{eff} is comparable to that of the best result obtained in semiconductor-based diodes in experiments for InP/(In,Ga)As system, performed under similar conditions (~ 0.2 A/W at 1 THz [20,21]). However, most of the physical parameters of the tunnel barriers used in our previous calclation[19], such as electron affinity and relative dielectric constant, were extracted from the experimetal I–V data of the MTJ having high R_DA (an order of kΩμm^2) with large A (36 μm^2)[16]. These values are actually three orders higher than desirable values for effective rectification of the THz wave. The next important step, therefore, is to fabricate and characterize the electrical properties of the MTJ with comparatively low R_DA and small A, and evaluate the feasibility in such cases.

In this study, we fabricated the epitaxial Fe(001)/ZnO(001)/MgO(001)/Fe(001) MTJs with R_DA of several Ωμm^2 and A ~ 0.01 μm^2. Based on a simple

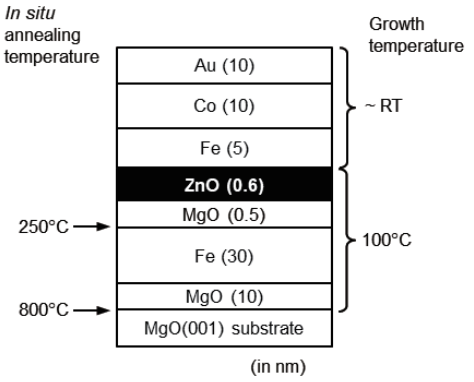

Fig. 1 Structure of the magnetic tunnel junction (MTJ) stack designed for this study. Growth and *in situ* annealing temperatures are also shown.

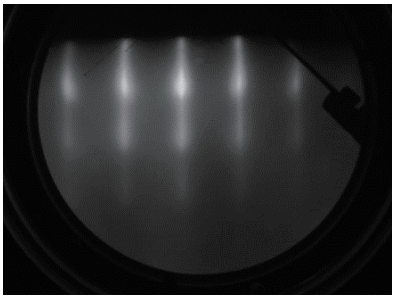

Fig. 2 Reflection high-energy electron diffraction image of the rock-salt type ZnO tunnel barrier ([100] azimuth of MgO substrate).

antenna-coupled diode model[7], we theoretically estimated β_{eff} of the MTJ prepared in this study, showing that it is possible to achieve the β_{eff} as high as 0.09 A/W at 1 THz under a zero-bias voltage at RT.

2. Experimental procedures

A MTJ film as shown in Fig. 1 was grown by molecular beam epitaxy in the identical growth chamber as used for the growth of epitaxial MTJs in our previous studies[16,20]. The MTJ film consisted of Au (5 nm) cap / Co (10 nm) pinned layer / Fe (5 nm) top electrode / ZnO (0.6 nm) upper tunnel barrier / MgO (0.5 nm) lower tunnel barrier / Fe (30 nm) bottom electrode / MgO (5 nm) buffer layer on a MgO(001) substrate, which is so called pseudo-spin valve structure. The t_{ZnO} and t_{MgO} were determined, in accordance with our theoretical calculation[19], so as to realize the maximum β_{eff} in this MTJ system. The ZnO upper tunnel barrier was confirmed to have identical reflection high-energy electron diffraction patterns (Fig. 2) to that of the MgO(001) lower tunnel barrier, indicating a single-crystalline with a metastable rock-salt type crystal structure. Detailed growth procedures and structural properties were described in our previous study.[18]

The film was patterned into tunnel junctions having elliptical shape using electron beam lithography technique. The lengths of the major and minor axes of the junctions were respectively 150 and 50 nm, corresponding to A = 0.0059 μm^2. Magnetoresistance (MR) and I–V characteristics of the junctions were measured at RT using conventional DC four and two probe methods, respectively. The MR ratio was defined as $(R_{AP}-R_P)/R_P$, where R_P and R_{AP} are the junction resistances between the two ferromagnetic (FM) electrodes with parallel (P) and antiparallel (AP) alignments, respectively. The magnetic fields were applied parallel to the major axis of the junction corresponding to the easy axis of the magnetization direction of the FM electrodes.

3. Results and discussions

3.1 Electrical transport measurements

Figure 3 shows a typical MR curve of the MTJs at RT. The observed MR ratio (43%) is close to the experimental value of epitaxial Fe/ZnO/MgO/Fe MTJs (51%) with thicker tunnel barrier layers (t_{ZnO} = 1.2 nm and t_{MgO} = 1.0 nm), grown at the same growth conditions in our previous study.[18] The MR curve always showed a low resistance state (i.e. the P state) at a zero-magnetic field, indicating that there is no significant magnetic coupling between the top and bottom FM electrodes. In Fig. 4, the first derivatives of the current (dI/dV) is displayed with regard to the bias voltage in the P state. The data were obtained from numerical differentiation of the I–V characteristics. The dI/dV–V curve indicated a notable asymmetry with respect to the polarity of the bias voltage, suggesting that the MTJ has a capability of square-low rectification at a zero-bias voltage.

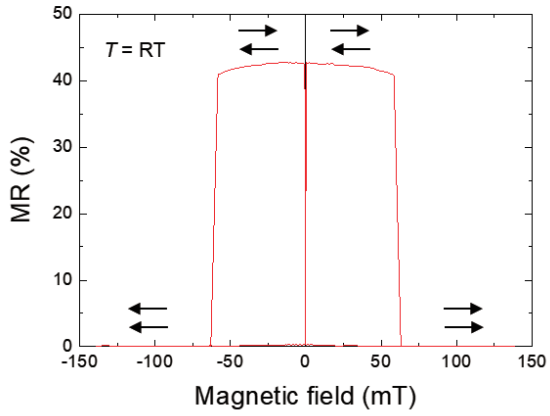

Fig. 3 Typical magnetoresistance (MR) curve of the Fe/ZnO/MgO/Fe MTJ at room temperature (RT) with a bias voltage of 10 mV. Arrows indicates the magnetization alignments in the top and bottom electrodes

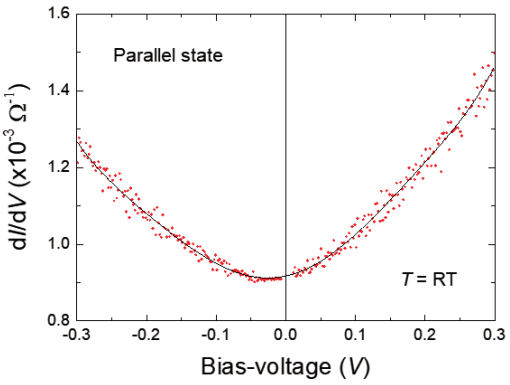

Fig. 4 (Red circles) Bias-V dependence of dI/dV of the Fe/ZnO/MgO/Fe MTJ at RT in the parallel (P) state of the magnetizations of the top and bottom electrodes. (Solid line) Polynomial fitting result to the dI/dV data.

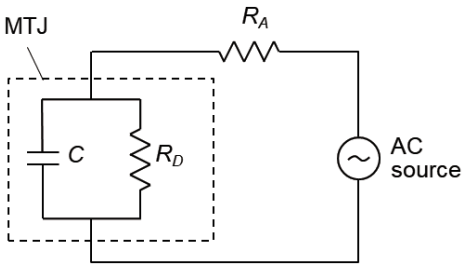

Fig. 5 Equivalent circuit of the antenna-coupled diode model[7] used in this study.

To calculate β_{eff}, we obtained two important parameters of R_DA [$\equiv (dI/dV)^{-1}A$] and β_0 [$\equiv (1/2)(d^2I/dV^2)/(dI/dV)$] from polynomial fittings to the dI/dV–V curve at a zero magnetic field (i.e. in the P state). Here, the parameter β_0 is equal to β_{eff} only when the resistance of the MTJ (R_D) completely matches with the internal real impedance (R_A), and also when the f of the incident electromagnetic wave is far below the cut-off frequency of the system. Therefore, β_0 does not necessarily represent the rectifying performance of the diode although it is in general referred to as the performance index. The obtained R_DA (6.3 Ωμm^2) and β_0 (0.20 A/W) were in good agreements with the theoretically estimated values in the identical MTJ (R_DA = 8.9 Ωμm^2 and β_0 = 0.23 A/W[19]), indicating that the MTJ prepared in this study justifies the design concept, and also fabricated precisely in line with the concept for the THz rectification.

3.2 Estimation of rectifying performance

The β_{eff} under a high-frequency condition is given by the following equation based on the antenna-coupled diode model (Fig. 5) [7],

$$\beta_{eff} = I_{dc}/P_{in} = 4\beta_0 x[1+2x+(1+q^2)x^2]^{-1}, \quad (1)$$

where I_{dc} is the rectified DC current, P_{in} is the power of incident electromagnetic wave. The variable x is the reduced junction resistance (= R_D/R_A), and q is the reduced frequency (= $2\pi fCR_A$). Note that x represents an impedance matching between the junction and the internal impedance whereas q is related to the RC time constant of the system. For R_D and β_0, we employed the experimental values in Fig. 4 (R_D =1.1 kΩ and β_0 = 0.20 A/W), so that the calculation was conducted in the P state. Inverse of junction capacitance (C^{-1}) for the present MTJ is given by $(\varepsilon_0\varepsilon_{ZnO}A/t_{ZnO})^{-1} + (\varepsilon_0\varepsilon_{MgO}A/t_{MgO})^{-1}$, where ε_0 is the dielectric constant, and ε_{ZnO} and ε_{MgO} are the relative dielectric constants of rock-salt ZnO (12[16]) and MgO (8.8[23]), respectively. Consequently, β_{eff} can be determined when f and R_A are given. Other possible factors of propagation or energy losses in high frequencies were not taken into account so that the calculated β_{eff} are the upper bounds in the MTJ.

The calculated β_{eff} are summarized in Figs. 6 and 7. As shown in Fig. 6, each β_{eff}–R_A curve took a maximum at a certain R_A which corresponds to the matching condition between R_D and R_A. For f = 100 GHz, a maximum β_{eff} (0.19 A/W) was approximately equal to β_0, indicating that the cut-off frequency is higher than 100 GHz. We confirmed no remarkable change in the β_{eff}–R_A relation below f = 100 GHz. When further increasing f, β_{eff} starts to decrease, especially in a high R_A regime. This is because the contribution of the RC time constant (the parameter q) to β_{eff} becomes significant in the high R_A regime. It would be possible to improve the cut-off frequency and thereby increase β_{eff} by reducing the R_DA down to a few Ωμm^2 [19]. Nevertheless, β_{eff} with the impedance matching condition still has a sizable value of 0.09 A/W at 1 THz which is approximately half the value of the best result obtained in experiments for semiconductor-based diodes (~ 0.2 A/W at 1 THz), performed under similar conditions[20,21]. Note that, as mentioned above, the β_{eff} calculated in the present MTJ are the upper bounds. Therefore, from practical

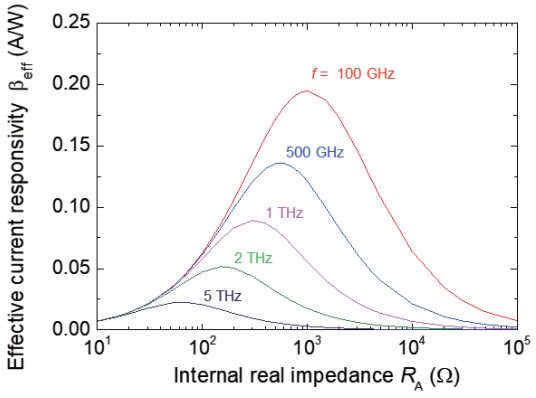

Fig. 6 Calculated effective current responsivity (β_{eff}) as a function of internal real impedance (R_A) for the Fe/ZnO/MgO/Fe MTJ prepared in this study. The values are plotted for various frequencies (f) of the input electromagnetic wave. The calculations were conducted at a zero-bias voltage in the P state.

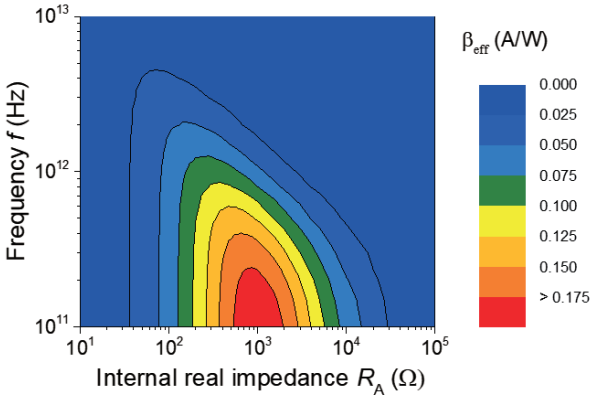

Fig. 7 Calculated β_{eff} of the Fe/ZnO/MgO/Fe MTJ as functions of f and R_A.

viewpoint, it is crucial to exhibit maximum rectifying performance by minimizing the propagation or energy losses in high frequencies as much as possible.

It should be noted that the rectified DC current and voltage in MTJ depend on the relative angle between the magnetizations of the two FM electrodes according to the changes in R_D and β_0. The phenomenon as such however, is impossible to accomplish in semiconductor-based diode and conventional MIM tunnel diode with a non-magnetic electrode(s). In other words, MTJ-based MIM diode provides novel functionality regarding manipulation of the rectified current/voltage by magnetic field in addition to the traditional rectifier. This unique function of MTJ may give rise to new device applications in high-frequency technology.

4. Conclusion

We fabricated fully epitaxial Fe/ZnO/MgO/Fe MTJs and theoretically estimated β_{eff} in a terahertz regime as a square-low detector. We obtained β_{eff} up to 0.09 A/W at 1 THz under a zero-bias voltage condition at RT, which is almost half the value of the best result obtained in experiments for semiconductor-based diodes, performed under similar conditions. The results strongly suggest that this MTJ system has a great potential for a rectifying element of a terahertz wave.

Acknowledgements We thank Dr. Akio Fukushima (AIST) for device fabrications and fruitful discussions. We also thank Dr. Hitoshi Kubota (AIST), and Dr. Masahiro Horibe (AIST) for valuable discussions.

References

1) H. J. Song, and T. Nagatsuma: *IEEE Trans. Terahz. Sci. Tech*, **1**, 256 (2011).
2) I. F. Akyildiz, J. M. Jornet, and C. Han: *Phys. Commun.* **12**, 16 (2014).
3) T. Nagatsuma, G. Ducournau, and C. C. Renaud: *Nat. Photo.*, **10**, 371 (2016).
4) D. M. Mittleman, G. Gupta, B. Neelamani, R. G. Baraniuk, J. V. Rudd, and M. Koch: *Appl. Phys. B*, **68**, 1085 (1999).
5) C. Jansen, S. Wietzke, O. Peters, M. Scheller, N. Vieweg, M. Salhi, N. Krumbholz, C. Jördens, T. Hochrein, and M. Koch: *Appl. Opt.*, **49**, E48 (2010).
6) A. Rogalski, and F. Sizov: *Opto-Electro. Rev.*, **19**, 346 (2011).
7) A. Sanchez, C. F. Davis, Jr., K. C. Liu, and A. Javan: *J. Appl. Phys.*, **49**, 5270 (1978).
8) S. Grover, and G. Moddel: *IEEE J. Photo*, **1**, 78 (2011).
9) S. Grover, and G. Moddel: *Sold State Electron.*, **67**, 94 (2012).
10) P. Periasamy, H. L. Guthrey, A. I. Abdulagatov, P. F. Ndione, J. J. Berry, D. S. Ginley, S. M. George, P. A. Parilla, and R. P. O'Hayre: *Adv. Mater.*, **25**, 1308 (2013).
11) N. Alimardani, and J. F. Conley, Jr: *Appl. Phys. Lett.*, **102**, 143501 (2013).
12) S. J. Byrnes, R. Blanchard, and F. Capasso: *Proc. Nat. Acad. Sci. U. S. A.*, **111**, 3927 (2014).
13) M. N. Gadalla, M. Abdel-Rahman, and A. Shamin: *Sci. Rep.*, **4**, 4270 (2014).
14) S. B. Herner, A. D. Weerakkody, A. Belkadi, and G. Moddel: *Appl. Phys. Lett.*, **110**, 223901 (2017).
15) D. Etro, L. E. Dodd, D. Wood, and C.Balocco: *Appl. Phys. Lett.*, **109**, 193110 (2016).
16) H. Saito, S. K. Narayananellore, N. Matsuo, N. Doko, S. Kon, Y. Yasukawa, H. Imamura, and S. Yuasa: *Phys. Rev. Appl.*, **11**, 064032 (2019).
17) Y. Uehara, A. Furuya, K. Sunaga, T. Miyajima, and H. Kanai: *J. Magn. Soc. Jpn.*, **34**, 311 (2010).
18) H. Tsukahara and H. Imamura: *Jpn. J. Appl. Phys.*, **58**, 010910 (2018).
19) H. Saito and H. Imamura: *Appl. Phys. Express*, **12**, 114003 (2019).
20) H. Ito and T. Ishibashi: *Appl. Phys. Express*, **9**, 092401 (2016).
21) H. Ito and T. Ishibashi: *Jpn. J. Appl. Phys.*, **56**, 014101 (2017).
22) N. Matsuo, N. Doko, T. Takada, H. Saito, and S. Yuasa: *Phys. Rev. Appl.*, **6**, 034011 (2016).
23) P. Padhan, P. LeClair, A. Gupta, K. Tsunakawa, and D. D. Djayaprawira: *Appl. Phys. Lett.*, **90**, 142105 (2007).

Received Dec. 6, 2019; Accepted Dec. 17, 2019

J. Magn. Soc. Jpn., **44**, 30-33 (2020)

Letter

Iron Loss and Hysteresis Properties of an Amorphous Ring Core at High Temperatures under Inverter Excitation

A. Yao

Department of Electrical and Computer Engineering, Toyama Prefectural University, *5180, Kurokawa, Imizu 939-0398, Japan*

Several researchers have recently studied high-temperature (HT) motor drive systems under harsh temperature environments. We experimentally and numerically investigate iron loss and the magnetic hysteretic properties of amorphous magnetic materials (AMM) at room temperature (RT) and HT under pulse width modulation (PWM) inverter excitation. We demonstrate that the iron loss of AMM core fed by PWM inverter decreases as temperature increases similar like in the sinusoidal case. In addition, the temperature dependence of the $B-H$ hysteresis curves of AMM under PWM inverter excitation relies not only on major loops but also on minor loops. Because the current at 300 °C is higher than that at RT, the torque of the motor with AMM at HT becomes large at a few operating points. To realize low iron loss of HT motor drive systems, it is important to reduce eddy current losses of AMM cores at HT under PWM inverter excitation compared with the cases at RT. These results facilitate further research in iron loss reduction of motor systems based on studies of magnetic properties at HT under PWM inverter excitation.

Key words: amorphous magnetic materials, high-temperatures, iron loss, hysteresis property, inverter

1 Introduction

Recently, several researchers have studied high-temperature (HT) motor drive systems under harsh temperature environments (*e.g.* fire sites, aerospace, and automotive)[1–5]. To perform the speed and torque control of these systems, pulse width modulation (PWM) inverters are commonly used[6–16]. When the PWM inverter excites the magnetic core used in the motor, the iron losses increase by 10%–50%[10] compared with the case under sinusoidal excitation owing to higher harmonic components. The temperature dependence of iron loss properties of conventional non-oriented (NO) electrical steel sheets (magnetic materials) have been demonstrated[4]. In addition, in the previous study[4], there has been no report on the loss repartition properties. To conduct fundamental research to develop high-efficiency motor drive system at HT, it is necessary to figure out magnetic characteristics of amorphous magnetic material (AMM) cores in HT environments under PWM inverter excitation.

To carry out iron loss reduction of the motor core particularly in high-frequency regions[15], a few researchers have studied the motor cores using AMM[15,17–28] that result in low iron losses compared with conventional non-oriented (NO) silicon steel. AMM is a suitable core for high-speed (HS) motor systems[21]. Further, in the HS motor system, the core is influenced by temperature. It is important to examine iron loss, hysteresis, and loss repartition (between the eddy current and the hysteresis losses) properties of AMM at HT excited by a PWM inverter.

Based on both experiments and numerical simulations, we examine the iron loss and magnetic hysteretic properties of AMM core at room temperature (RT) and 300 °C (HT) under PWM inverter excitation. This paper reports on the experimental iron loss and hysteretic properties of a ring specimen with AMM under a wide temperature range (RT and HT) condition. Here, the play model with the Cauer circuit[4,5,29–34] is used for numerical simulations. We discuss the loss repartition between the eddy current and the hysteresis losses at RT (about 27 °C) and 300 °C.

2 Experimental and Numerical Methods

Figure 1 shows the experimental system employed to measure the iron loss properties of a ring specimen with AMM (SA1) under a wide temperature range condition. The AMM alloy ribbons are laminated and then impregnated with acrylic resin to fabricate a block core. This laminated block core is cut in the shape of a ring core. The AMM ring core with an outer and inner diameter of 102 mm and 127 mm, respectively, is constructed. The space factor ξ_{sf} of the AMM core is approximately 93.5 %. The primary and secondary coils are wound into the ring core. The ring specimen with AMM is set in the oven to examine temperature dependence of iron loss properties. In this study, this ring specimen with AMM is set to either RT or 300 °C. More details of the ring specimen can be found in Ref.[35].

Here, we measure iron loss characteristics of the AMM ring specimen at RT and HT excited by a PWM inverter (MWINV-9R122C, Myway). The iron loss W_{ring} of the ring specimen with

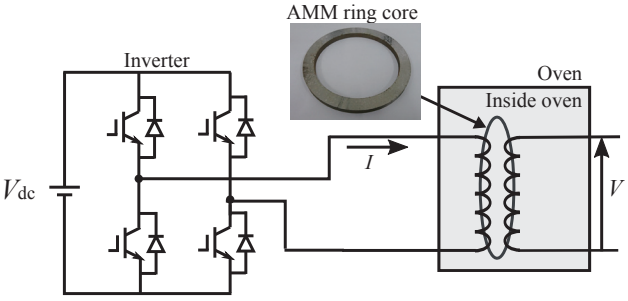

Fig. 1 Schematic of iron loss measurement system of AMM ring specimen excited by PWM inverter.

AMM is described by [4,5)]

$$W_{\mathrm{ring}} = \frac{1}{T\rho}\int H\mathrm{d}B, \tag{1}$$

where H denotes the magnetic field intensity, B is the magnetic flux density, T (= 0.02 s) is the period, and ρ (= 7180 kg/m^3) is the density of AMM. Here, H and B are represented as $N_1 I/l$ and $\int Vdt/(N_2 S\xi_{\mathrm{sf}})$, respectively, where N_1 (= 103) denotes the number of turns in the exciting coil, I is the current flowing in the primary coil of the ring core, l (= 0.36 m) is the magnetic path length, V is the voltage of the secondary coil, N_2 (= 103) is the number of turns of the secondary coil, and S (= 87.5 mm^2) is the cross-sectional area of the ring core. The primary and the secondary windings are set to have the same number of turns because it is important to measure higher harmonic (small voltage) waves and to suppress the measurement error of the magnetic flux density.

In this study, to simulate numerical $B-H$ hysteresis curves of the ring specimen fed by a PWM inverter under a wide temperature range (RT and HT) condition, we use the play model with the Cauer circuit as a dynamic hysteresis model (See Refs.[4,5,32,33)] for details regarding the play model with the Cauer circuit.). The $B-H$ hysteresis curve in the play model with the Cauer circuit is given by [4,5,32)]

$$H_{\mathrm{AC}}(B) = H_{\mathrm{DC}}(B) + \frac{7(B^k - B^{k-1}) + 2L' h_2^{k-1}}{7R_{\mathrm{E}}\Delta t + 2L'} + \frac{3L'(h_2^k - h_2^{k-1})}{35R_{\mathrm{E}}\Delta t}, \tag{2}$$

$$R_{\mathrm{E}} = \frac{12}{\alpha\sigma d^2}, \tag{3}$$

where $H_{\mathrm{DC}}(B)$ denotes the DC hysteresis curve calculated by the play model, σ is the electrical conductivity of AMM, Δt is the time division, d is the thickness of AMM, k is the step number, R_E is the resistance to express eddy currents, L' is the equivalent inductance to represent the magnetic flux caused by eddy currents, and α is the anomaly factor to represent anomalous eddy currents. Here, L' and α are fitting parameters. In our study, by adjusting L', the numerical iron loss of the minor loop is fitted to the measured loss. Then, α is adjusted to equalize the numerical loss to the experimental one.

In our numerical simulations, L' at the carrier frequencies of 1, 5, 10, 15, and 20 kHz is obtained as about 10, 4, 2, 0.8, and 0.4 mH, respectively, (8, 3, 1, 0.6, and 0.4 mH) at RT (300 °C). It is thought that the ratio of iron loss based on L' in the minor loops changes as temperature increases. α at f_{c} = 1, 5, 10, 15, and 20 kHz is about 278, 274, 260, 255, and 253 at RT (202, 200, 199, 197, and 194 at 300 °C), respectively. In our study, based on the sheet tests to expose the ambient temperature variations in the oven, σ at RT and 300 °C is 7.7×10^5 [36)] and 7.3×10^5 S/m, respectively. The maximum magnetic flux density B_{max}, fundamental frequency, modulation index, and switching dead time are set to 0.8 T, 50 Hz, 0.7, and 3.5 μs, respectively. Figure 2 shows the experimental DC hysteresis curves ($H_{\mathrm{DC}}(B)$) without harmonics at each temperature (RT and HT). These experimental DC hysteresis curves [4,32)] at each temperature are used to build the play model. Five carrier frequencies f_{c} (1, 5, 10, 15, and 20 kHz) are tested.

3 Results and Discussion

Figure 3 shows experimental and numerical $B-H$ hysteresis curves at RT and 300 °C of the AMM ring core, excited by the PWM inverter with a carrier frequency of 5 kHz. The calculated $B-H$ curves are almost consistent with the experimental results. Here, the iron losses of the AMM ring fed by PWM inverter at f_{c} = 5 kHz are about 0.33 W/kg at RT and 0.20 W/kg at 300 °C. The iron loss at 300 °C is smaller than that at RT.

Fig. 3(c) shows that the coercivity at RT is larger than that at 300 °C. As shown in Fig. 2, the coercivity of the DC hysteresis loops at HT becomes small because it is assumed that there appears thermal fluctuation (thermal energy) at HT. The coercivity also becomes small when the eddy current loss due to low conductivity at HT decreases for $B-H$ hysteresis curves. In Fig. 2, the amorphous ring core at RT and HT exhibits the hysteresis loss at 0.8 T of about 4.6 and 2.6 mJ/kg, respectively. Therefore, it is considered that, owing to thermal fluctuation, the hysteresis losses decrease [37)] at HT [4)]. As mentioned above, the electrical conductivity at 300 °C is smaller than that at RT. The classical eddy current loss is proportional to the electrical conductivity[4,38,39)]. It is considered that the anomalous eddy current losses caused by magnetic domain wall movement decrease due to low conductivity at HT. Owing to the small electrical conductivity at HT, the eddy current loss decreases as temperature increases.

The torque of the motor depends on the current (magnetic field intensity) through the motor core. Figure 3(b) shows that the magnetic field intensity (current) at 300 °C is larger than that at RT at a few operating points for the same magnetic flux density. As shown in Fig. 2, the magnetic field intensity of DC hysteresis curves near B_{max} at HT is also larger than that at RT. It is considered that due to the thermal fluctuation the energy for aligning the magnetic moment near B_{max} increases with increasing tem-

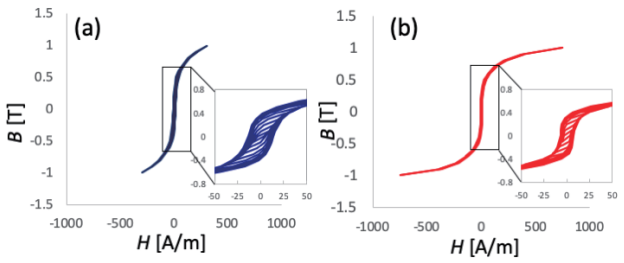

Fig. 2 Experimental DC hysteresis curves (B_{max} = 0.1, 0.2, 0.3, 0.4, 0.5, 0.6, 0.7, 0.8, 0.9, and 1.0 T) used in our numerical simulations at each temperature: (a) RT and (b) 300 °C

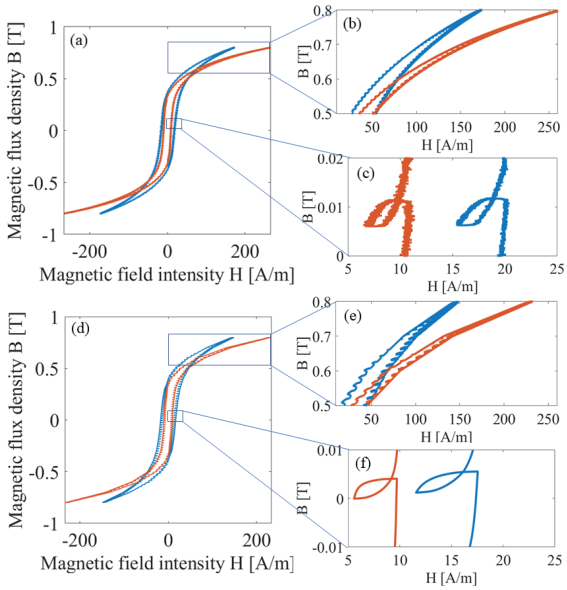

Fig. 3 B–H hysteresis curves of AMM ring at RT and 300 °C fed by PWM inverter at B_{max} = 0.8 T and f_c = 5 kHz. Blue and red lines denote curves at RT and 300 °C, respectively. The enlarged view shows curves near maximum magnetic field intensity and minor loops of $B-H$ curves: (a), (b), and (c) shows experimental results, and (d), (e), and (f), the corresponding numerical results.

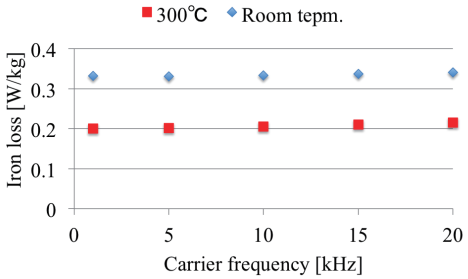

Fig. 4 Iron loss properties of AMM ring specimen with respect to carrier frequency at B_{max} = 0.8 T. Blue (red) points denote results at RT (300 °C). Carrier frequencies f_c is set to 1, 5, 10, 15, and 20 kHz.

peratures. Because the current at 300 °C increases, the torque of the motor with AMM increases at a few operating points.

Fig. 3(c) shows that the area of the minor loop is about 8.4 and 7.9 mJ/m^3 at RT and 300 °C, respectively. The area of the minor loops of the AMM ring core decreases as temperature increases (See Ref.[9] for details of the minor loops.). This is because it is considered that, due to the influence of heat, the hysteresis and eddy current losses decrease as temperature increases. The temperature dependence of the $B-H$ hysteresis curves of AMM ring core relies not only on major loop but also on minor loops.

Figure 4 shows the iron losses as a function of carrier frequency of the AMM ring specimen at RT and 300 °C under PWM inverter excitation. For every tested carrier frequency, the iron losses of the inverter-excited AMM ring decrease as temperature

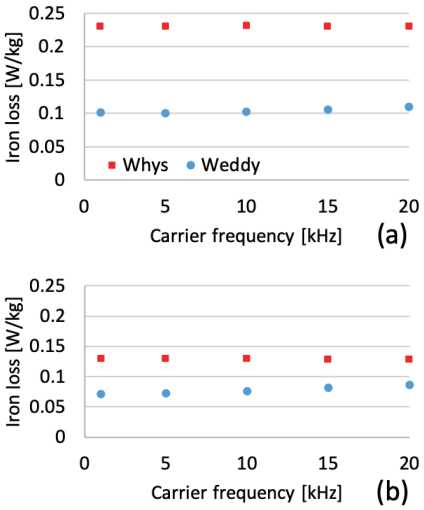

Fig. 5 Iron loss repartition between the hysteresis (red points, W_{hys}) and eddy current (blue points, W_{eddy}) losses under PWM inverter excitation at B_{max} = 0.8 T with Eq. (4): (a) RT. (b) 300 °C.

increases. The iron loss at high carrier frequency becomes larger than that at low carrier frequency under this operating point at HT. The relationship between iron losses and higher carrier frequency at HT will be examined in a future presentation.

Figure 5 shows the loss repartition between the eddy current and the hysteresis losses at RT and 300 °C under PWM inverter excitation. Here, the hysteresis loss W_{hys} is calculated at σ = 0 with Eqs. (2) and (3). Then, the eddy current loss W_{eddy} is obtained by[40]

$$W_{eddy} = W_{ring} - W_{hys}. \tag{4}$$

We can achieve highly accurate calculations for loss separation because fitting parameters and the experimental DC hysteresis curves are used in our numerical simulations. The average W_{eddy} of the inverter-excited AMM rings at RT and at 300 °C accounts for 31% and 37% of the total iron losses, respectively. The ratio of W_{eddy} to W_{ring} at 300 °C is larger than that at RT. To realize low iron loss of HT and HS motor drive systems, it is important to reduce eddy current losses of the AMM cores at HT excited by inverter compared with the cases at RT. In addition, understanding the dynamic hysteresis properties also leads to simulating accurate motor loss characteristics[41]. These results facilitate further research in loss reduction of HT and HS motor systems based on studies of magnetic properties under PWM inverter excitation.

4 Conclusion

Based on both experiments and numerical simulations, this study for the first time investigated iron loss and hysteretic properties of AMM ring core at RT and 300 °C under PWM inverter excitation. Owing to low electrical conductivity and thermal fluctuation at HT, the iron loss of AMM core fed by PWM inverter decreased as temperature increased similar like in the sinusoidal

case. The torque of the motor with AMM became large at a few operating points under the same magnetic flux density. This was because the current (magnetic field intensity) at 300 °C was larger than that at RT at a few operating points. To realize low iron loss of HT and HS motor drive systems, it was important to reduce eddy current losses of AMM cores at HT excited by inverter compared with the cases at RT. These results facilitate further research regarding the loss reduction of HT and HS motor systems based on the iron loss and hysteretic properties of AMM core at HT under PWM inverter excitation. The future work will address further numerical and experimental studies under a wider range of magnetic flux density and temperatures to reveal general magnetic properties of AMM at HT under inverter excitation.

Acknowledgment This work was partly supported by the JSPS KAKENHI ♯18K13749, JST OPERA ♯JPMJOP1841, JFE 21st Century Foundation, Kansai Research Foundation, Takeuchi Foundation, and Nagamori Foundation Research Grant.

References

1) L. Burdet: Ph.D. dissertation, Citeseer (2006).
2) T. D. Kefalas and A. G. Kladas: *IEEE Trans. Ind. Electron.*, **61**, 4404 (2014).
3) A. Yao, A. Adachi, and K. Fujisaki: *Proc. IEMDC*, 1 (IEEE, 2017).
4) A. Yao, S. Odawara, and K. Fujisaki: *IEEJ J. Ind. Appl.*, **7**, 298 (2018).
5) A. Yao and T. Hatakeyama: *J. Magn. Soc. Jpn.*, **43**, 46 (2019).
6) A. Boglietti, P. Ferraris, M. Lazzari, and M. Pastorelli: *IEEE Trans. Magn.*, **32**, 4884 (1996).
7) A. Boglietti, P. Ferraris, M. Lazzari, and F. Profumo: *IEEE Trans. Magn.*, **27**, 5334 (1991).
8) A. Boglietti, P. Ferraris, M. Lazzari, and M. Pastorelli: *IEEE Trans. Magn.*, **31**, 4250 (1995).
9) M. Kawabe, T. Nomiyama, A. Shiozaki, H. Kaihara, N. Takahashi, and M. Nakano: *IEEE Trans. Magn.*, **48**, 3458 (2012).
10) K. Fujisaki and S. Liu: *J. Appl. Phys.*, **115**, 17A321 (2014).
11) S. Odawara, K. Fujisaki, and F. Ikeda: *IEEE Trans. Magn.*, **50**, 1 (2014).
12) T. Taitoda, Y. Takahashi, and K. Fujiwara: *IEEE Trans. Magn.*, **51**, 1 (2015).
13) A. Yao, K. Tsukada, S. Odawara, K. Fujisaki, Y. Shindo, N. Yoshikawa, and T. Yoshitake: *AIP Adv.*, **7**, 056618 (2017).
14) A. Yao and K. Fujisaki: *Proc. LDIA2017*, 1 (IEEJ, 2017).
15) A. Yao, T. Sugimoto, S. Odawara, and K. Fujisaki: *AIP Adv.*, **8**, 056804 (2018).
16) A. Yao, T. Sugimoto, S. Odawara, and K. Fujisaki: *IEEE Trans. Magn.*, **54**, 1 (2018).
17) N. Denis, Y. Kato, M. Ieki, and K. Fujisaki: *AIP Adv.*, **6**, 055916 (2016).
18) S. Okamoto, N. Denis, Y. Kato, M. Ieki, and K. Fujisaki: *IEEE Trans. Ind. Appl.*, **52**, 2261 (2016).
19) M. Dems and K. Komeza: *IEEE Trans. Ind. Electron.*, **61**, 3046 (2014).
20) A. Chiba, H. Hayashi, K. Nakamura, S. Ito, K. Tungpimolrut, T. Fukao, M. A. Rahman, and M. Yoshida: *IEEE Trans. Ind. Appl.*, **44**, 699 (2008).
21) Z. Wang, Y. Enomoto, R. Masaki, K. Souma, H. Itabashi, and S. Tanigawa: *Proc. ICPE & ECCE*,1940 (IEEE, 2011).
22) G. S. Liew, W. L. Soong, N. Ertugrul, and J. Gayler: *Proc. AUPEC*, 1 (IEEE, 2010).
23) Z. Wang, Y. Enomoto, M. Ito, R. Masaki, S. Morinaga, H. Itabashi, and S. Tanigawa: *IEEE Trans. Magn.*, **46**, 570 (2010).
24) Z. Wang, R. Masaki, S. Morinaga, Y. Enomoto, H. Itabashi, M. Ito, and S. Tanigawa: *IEEE Trans. Ind. Appl.*, **47**, 1293 (2011).
25) Y. Enomoto, M. Ito, H. Koharagi, R. Masaki, S. Ohiwa, C. Ishihara, and M. Mita: *IEEE Trans. Magn.*, **41**, 4304 (2005).
26) T. Fan, Q. Li, and X. Wen: *IEEE Trans. Ind. Electron.*, **61**, 4510 (2014).
27) R. Kolano, K. Krykowski, A. Kolano-Burian, M. Polak, J. Szynowski, and P. Zackiewicz: *IEEE Trans. Magn.*, **49**, 1367 (2013).
28) A. Yao, T. Sugimoto, and K. Fujisaki: *J. Magn. Soc. Jpn.*, **43**, 42 (2019).
29) J. H. Krah: *IEEE Trans. Magn.*, **41**, 1444 (2005).
30) Y. Shindo and O. Noro: *IEEJ Trans. Fund. Mater.*, **134**, 173 (2014).
31) Y. Shindo, T. Miyazaki, and T. Matsuo: *IEEE Trans. Magn.*, **52**, 1 (2016).
32) S. Odawara, K. Fujisaki, T. Matsuo, and Y. Shindo: *IEEJ Trans. Ind. Appl.*, **135**, 1191 (2015).
33) T. Miyazaki, T. Mifune, T. Matsuo, Y. Shindo, Y. Takahashi, and K. Fujiwara: *J. Appl. Phys.*, **117**, 17D110 (2015).
34) S. Odawara and K. Fujisaki: *IEEE Trans. Magn.*, **54**, 1 (2018).
35) A. Yao, K. Tsukada, and K. Fujisaki: *IEEJ J. Ind. Appl.*, **7**, 321 (2018).
36) *Amorphous alloy ribbon catalog No. HJ-B10-B*. Hitachi Metals, Ltd. (in Japanese).
37) N. Takahashi, M. Morishita, D. Miyagi, and M. Nakano: *IEEE Trans. Magn.*, **46**, 548 (2010).
38) D. Singh, P. Rasilo, F. Martin, A. Belahcen, and A. Arkkio: *IEEE Trans. Magn.*, **51**, 1 (2015).
39) *To understand electrical steel sheets*. Nippon Steel and Sumitomo Metal Corporation (2012) (in Japanese).
40) S. Odawara and K. Fujisaki: *The papers of Technical Meeting, MD, IEE Japan*, **MD-18-035**, 49 (2018).
41) Y. Takeda, Y. Takahashi, K. Fujiwara, A. Ahagon, and T. Matsuo: *IEEE Trans. Magn.*, **51**, 1 (2015).

Recieved Sep. 4, 2019; Revised Oct. 6, 2019; Accepted Nov. 26, 2019

J. Magn. Soc. Jpn., **44**, 34-39 (2020)

<Paper>

Information Stability in Three-Dimensional Heat-Assisted Magnetic Recording

T. Kobayashi, Y. Nakatani*, and Y. Fujiwara

Graduate School of Engineering, Mie Univ., *1577 Kurimamachiya-cho, Tsu 514-8507, Japan*

*Graduate School of Informatics and Engineering, Univ. of Electro-Communications, *1-5-1 Chofugaoka, Chofu 182-8585, Japan*

The anisotropy constant ratio K_u/K_{bulk} necessary for information stability in three-dimensional heat-assisted magnetic recording (3D HAMR) of 2 Tbpsi (total density of 4 Tbpsi) is evaluated by employing a bit error rate calculation using grain error probability. The minimum K_u/K_{bulk} value of a high Curie temperature (HC) layer is limited by the information stability in the HC layer while writing in a low Curie temperature (LC) layer, and a high K_u/K_{bulk} is necessary for the HC layer. The minimum K_u/K_{bulk} value of the LC layer is limited by the information stability in the LC layer for 10 years of archiving, and a high K_u/K_{bulk} is also necessary for the LC layer since the anisotropy constant of the LC layer is intrinsically low at the storage temperature due to its low Curie temperature. At 9 grains/bit, the K_u/K_{bulk} values required for 3D HAMR are 0.85 and 0.86 for the HC and LC layers, respectively, taking account of certain variations, namely, standard deviations of 2 % for the Curie temperature and 15 % for the grain size.

Key words: 3D HAMR, anisotropy constant ratio, bit error rate, probability

1. Introduction

Heat-assisted magnetic recording (HAMR) is a promising candidate as a next generation magnetic recording method capable of operating beyond the trilemma limit[1]. HAMR is a recording method in which the medium is heated to reduce coercivity during the writing period. We have introduced a HAMR design parameter, namely, the medium anisotropy constant ratio K_u/K_{bulk} [2] in place of the medium anisotropy constant K_u since the K_u value is a function of the medium Curie temperature T_c. K_u/K_{bulk} is the intrinsic ratio of the medium K_u to bulk FePt K_u regardless of T_c where FePt is a candidate HAMR medium material thanks to its large K_u and relatively low T_c. A low T_c is advantageous for writing in HAMR. However, a larger K_u/K_{bulk} is needed for a low T_c medium for 10 years of archiving[3]. And a medium with a high K_u/K_{bulk}, *e.g.* 0.6 – 1.0, is difficult to manufacture regardless of T_c (Figure 2 (a) in reference 4)).

Three-dimensional magnetic recording is useful for increasing the recording capacity. Three-dimensional HAMR (3D HAMR) has been proposed[5] where the medium consists of a high Curie temperature (HC) layer and a low Curie temperature (LC) layer with no interlayer exchange-coupling. With 3D HAMR, after writing data in the HC layer, other data can be written in the LC layer by employing lower temperature heating.

In this paper, we discuss the information stability in the HC layer while writing in the LC layer, and the information stability in the HC and LC layers for 10 years of archiving for 3D HAMR at 2 Tbpsi (total density of 4 Tbpsi) employing a K_u/K_{bulk} value.

2. Calculation Method

The anisotropy constant ratio K_u/K_{bulk} needed for information stability was evaluated by employing a bit error rate calculation using the grain error probability P

$$P = 1 - \exp\left(-f_0 t \exp\left(-K_\beta\right)\right),$$

$$K_\beta = \frac{K_{um} V_m}{kT} \cdot \left(\frac{K_u}{K_{um}}\right) \cdot \left(\frac{D}{D_m}\right)^2 \cdot \left(1 + \frac{H_w}{H_k}\right)^2$$

$$\left(|H_w| < H_k\right) \tag{1}$$

under a writing field $H_w < 0$ antiparallel to the recording direction where f_0, t, K_{um}, V_m, k, T, K_u, D, and H_k are the attempt frequency, time, the mean grain anisotropy constant, the grain volume for mean grain size D_m, the Boltzmann constant, temperature, the grain anisotropy constant, the grain size, and the grain anisotropy field, respectively[3].

The attempt frequency f_0 has been calculated as

$$f_0 = \frac{\gamma\alpha}{1+\alpha^2} \sqrt{\frac{M_s H_k^3 V}{2\pi kT}} \left(1 - \left(\frac{H_w}{H_k}\right)^2\right)\left(1 + \frac{H_w}{H_k}\right)$$

$$\left(|H_w| < H_k\right) \tag{2}$$

where γ, α, M_s, and V are the gyromagnetic ratio, the Gilbert damping constant, the grain magnetization, and the grain volume, respectively[6].

The temperature dependence of M_s was determined by employing a mean field analysis[7], and that of K_u

was assumed to be proportional to M_s^2[8]. The T_c value was adjusted by the Cu simple dilution of $(Fe_{0.5}Pt_{0.5})_{1-z}Cu_z$. $M_s(T_c, T)$ is a function of T_c and T, and $M_s(T_c = 770\ \mathrm{K}, T = 300\ \mathrm{K}) = 1000$ emu/cm^3 was assumed for FePt (Cu composition $z = 0$). $K_u(T_c, K_u/K_{bulk}, T)$ is a function of T_c, K_u/K_{bulk}, and T where K_u/K_{bulk} is the intrinsic ratio of the medium $K_u(T_c, K_u/K_{bulk}, T)$ to bulk FePt $K_u(T_c, K_u/K_{bulk} = 1, T)$ at the same T_c and T, namely,

$$K_u/K_{bulk} = \frac{K_u(T_c, K_u/K_{bulk}, T)}{K_u(T_c, K_u/K_{bulk} = 1, T)}. \quad (3)$$

Although $K_u(T_c, K_u/K_{bulk}, T)$ is a function of T_c and T, K_u/K_{bulk} is independent of T_c and T. A medium with a high K_u/K_{bulk} is difficult to manufacture. $K_u(T_c = 770\ \mathrm{K}, K_u/K_{bulk} = 1, T = 300\ \mathrm{K}) = 70$ Merg /cm^3 was assumed for FePt ($z = 0$).

The recording density is 2 Tbpsi (total density of 4 Tbpsi), and the area S of a bit is 323 nm^2. The medium was assumed to be granular in which each bit had n grains/bit. The mean grain size D_m was determined by

$$D_m = \sqrt{\frac{S}{n}} - \Delta \quad (4)$$

where the non-magnetic spacing Δ was assumed to be 1 nm. The D_m values were 8.0 and 5.0 nm for n values of 4 and 9 grains/bit, respectively. The grain volume V_m for D_m was $D_m \times D_m \times h$ where h is the grain height.

We assumed that the grain size distribution was log-normal with a standard deviation σ_D, and that the Curie temperature distribution was normal with a mean Curie temperature T_{cm} and standard deviation σ_{Tc}. No intrinsic distribution of K_u was assumed. However, there was a fluctuation of K_u caused by σ_{Tc}.

The bit error rate was calculated using each grain error probability P_i[3]. For example, for 4 grains/bit, the 1 grain-error bit error rate ${}_4\mathrm{bER}_1$ is expressed as

$${}_4\mathrm{bER}_1 = Er_1P_1(1-P_2)(1-P_3)(1-P_4) + \cdots + Er_4(1-P_1)(1-P_2)(1-P_3)P_4, \quad (5)$$

the 2 grain-error bit error rate ${}_4\mathrm{bER}_2$

$${}_4\mathrm{bER}_2 = Er_{12}P_1P_2(1-P_3)(1-P_4) + \cdots + Er_{34}(1-P_1)(1-P_2)P_3P_4, \quad (6)$$

the 3 grain-error bit error rate ${}_4\mathrm{bER}_3$

$${}_4\mathrm{bER}_3 = Er_{123}P_1P_2P_3(1-P_4) + \cdots + Er_{234}(1-P_1)P_2P_3P_4, \quad (7)$$

and the 4 grain-error bit error rate ${}_4\mathrm{bER}_4$

$${}_4\mathrm{bER}_4 = P_1P_2P_3P_4 \quad (8)$$

where

$$Er_j = 1, \text{ if } \frac{\sum_i M_{si}(T_{ci}, T)D_i^2}{n \cdot M_s(T_{cm}, T)D_m^2} \le 0.5, \text{ and}$$

$$Er_j = 0, \text{ if } \frac{\sum_i M_{si}(T_{ci}, T)D_i^2}{n \cdot M_s(T_{cm}, T)D_m^2} > 0.5. \quad (9)$$

Errors occur in some grains of a bit. We assume that if the surface magnetic charge $\sum M_{si}(T_{ci}, T)D_i^2$ of the grains where the magnetization turns in the recording direction is more than 50 % (signal threshold) of the total surface magnetic charge $n \cdot M_s(T_{cm}, T)D_m^2$ in a bit, the bit is error free where M_{si}, T_{ci}, and D_i are the magnetization, the Curie temperature, and the grain size of the i-th grain, respectively.

In conclusion, the total bit error rate ${}_4\mathrm{bER}$ is the summation of each bit error rate ${}_4\mathrm{bER}_k$ as follows

$${}_4\mathrm{bER} = \sum_k {}_4\mathrm{bER}_k. \quad (10)$$

To simplify the model calculation, neither the demagnetizing nor the magnetostatic fields were considered in this paper. The problem posed by these fields is a future subject.

3. Calculation Results

3.1 Information stability in HC layer while writing in LC layer

First, we discuss the information stability in a high Curie temperature T_{HC} (HC) layer while writing in a low Curie temperature T_{LC} (LC) layer. The calculation conditions are summarized in Table 1. The calculation bit number was 10^7.

Table 1 Calculation conditions for information stability in an HC layer while writing in an LC layer.

Recording density (Tbpsi)	2
Total density (Tbpsi)	4
Non - magnetic spacing Δ (nm)	1
Signal threshold	0.5
Bit number (bits)	10^7

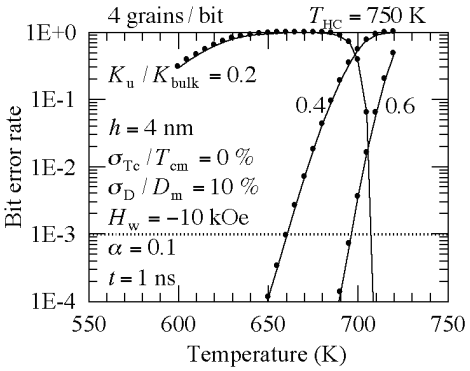

Fig. 1 Temperature dependence of bit error rate for various anisotropy constant ratios K_u/K_{bulk}.

Figure 1 shows the temperature dependence of the bit error rate (bER) for various K_u/K_{bulk} values under the conditions indicated in the figure.

When the error level is low, Eq. (1) can be approximated as Eq. (11).

$$P \approx f_0 t \exp\left(-\frac{K_{um}V_m}{kT}\cdot\left(\frac{K_u}{K_{um}}\right)\cdot\left(\frac{D}{D_m}\right)^2\cdot\left(1+\frac{H_w}{H_k}\right)^2\right). \quad (11)$$

The variables in an exponential function become parameters with a strong impact on bER, for example, T. Furthermore, $K_{um}(T_c, K_u/K_{bulk}, T)$ also has a strong effect. The bER increases rapidly as the temperature increases or K_u/K_{bulk} decreases.

When K_u/K_{bulk} = 0.2, the bER apparently becomes zero at about 710 K where $|H_w| = H_k$, $1+H_w/H_k \to 0$ in Eq. (2), and f_0 becomes zero. Equations (1) and (2) cannot be applied around the temperature where $|H_w| = H_k$ since the magnetization reversal is not a matter of probability. When K_u/K_{bulk} = 0.2 and 650 K, bER is almost 1, and K_u/K_{bulk} of 0.2 is insufficient for information stability at high temperature. Although a medium with K_u/K_{bulk} > 0.6 is difficult to manufacture, K_u/K_{bulk} > 0.6 is preferable for the information stability at 650 K when we take account of grain size and Curie temperature variations (see Fig. 10 (a)). It may be necessary to increase K_u/K_{bulk}.

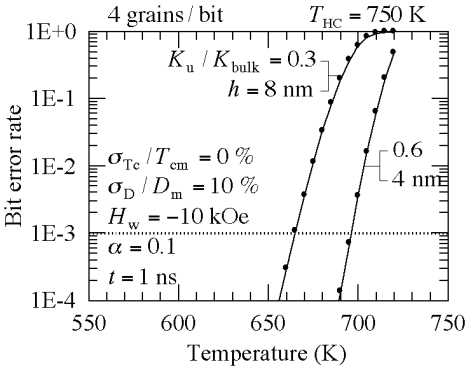

Fig. 2 Temperature dependence of bit error rate for (K_u/K_{bulk} = 0.6, h = 4 nm) and (K_u/K_{bulk} = 0.3, h = 8 nm) combinations.

Although K_u/K_{bulk} > 0.28 is necessary for 10 years of archiving (see Table 3), K_u/K_{bulk} > 0.6 is required for information stability while writing in the LC layer. Therefore, we consider the grain height h to reduce K_u/K_{bulk}. Figure 2 shows the temperature dependence of the bER for (K_u/K_{bulk} = 0.6, h = 4 nm) and (K_u/K_{bulk} = 0.3, h = 8 nm) combinations. The $K_uV = K_u(D^2h)$ values are the same for both combinations. However, the bER for (K_u/K_{bulk} = 0.3, h = 8 nm) is higher since the $H_k = 2K_u/M_s$ value in Eq. (11) for (K_u/K_{bulk} = 0.3, h = 8 nm) is lower. When H_w = 0, (K_u/K_{bulk} = 0.6, h = 4 nm) and (K_u/K_{bulk} = 0.3, h = 8 nm) are equivalent for the information stability. However, when $H_w \neq 0$, K_u/K_{bulk} cannot be halved by doubling the height h.

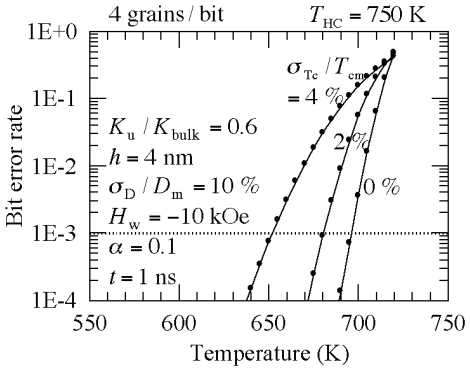

Fig. 3 Temperature dependence of bit error rate for various standard deviations σ_{Tc}/T_{cm} of Curie temperature.

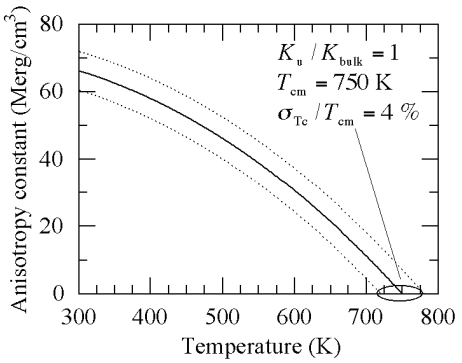

Fig. 4 Temperature dependence of anisotropy constant.

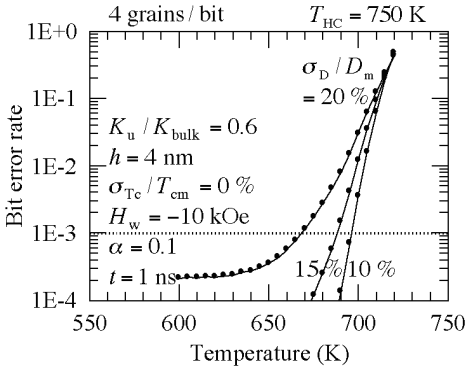

Fig. 5 Temperature dependence of bit error rate for various standard deviations σ_D/D_m of grain size.

The HAMR medium has various variations, for example, the Curie temperature and grain size variations. Figure 3 shows the temperature dependence of the bER for various σ_{Tc}/T_{cm} values. When σ_{Tc}/T_{cm} = 4 %, the bER is particularly high.

This is explained using the temperature dependence of K_u as shown in Fig. 4. The T_c variation causes the K_u fluctuation (K_u/K_{um}) in Eq. (11). The standard

deviation σ_{Ku}/K_{um} of K_u caused by σ_{Tc}/T_{cm} of 4 % is only 9 % at 300 K. Therefore, the existence of σ_{Tc}/T_{cm} = 4 % has a weak effect for 10 years of archiving at 300 K[3]. However, σ_{Ku}/K_{um} reaches about 31 % at 650 K. Therefore, a small Curie temperature variation is required for 3D HAMR.

The temperature dependence of the bER for various σ_D/D_m values is shown in Fig. 5. The change in D caused by σ_D corresponds to $(D/D_m)^2 = \left((D_m-\sigma_D)/D_m\right)^2$ in Eq. (11). Therefore, a σ_D/D_m of 20 % has a strong impact on the bER. And a small grain size variation is also required for 3D HAMR.

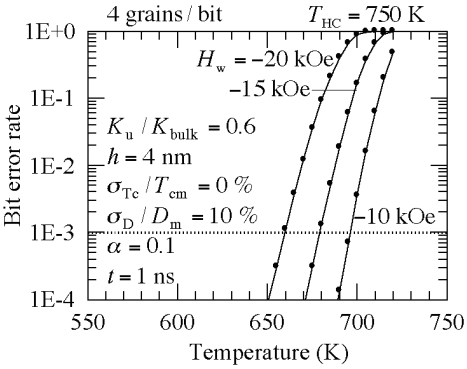

Fig. 6 Temperature dependence of bit error rate for various writing fields H_w.

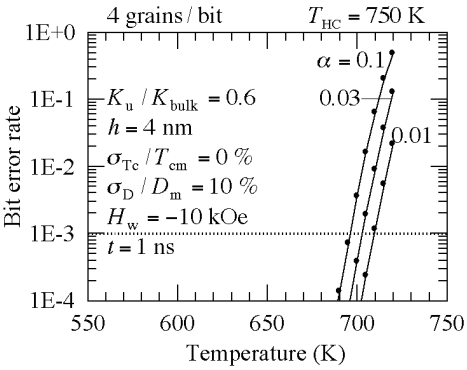

Fig. 7 Temperature dependence of bit error rate for various Gilbert damping constants α.

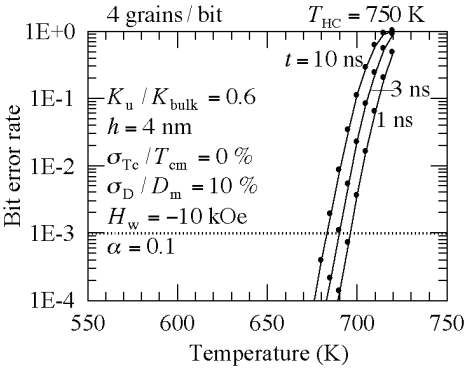

Fig. 8 Temperature dependence of bit error rate for various times t.

As described below in 3.3, a high K_u/K_{bulk} is required in the LC layer for 10 years of archiving. And a relatively high field is necessary while writing in the LC layer due to its high K_u/K_{bulk}[4]. Figure 6 shows the temperature dependence of the bER for various H_w values while writing in the LC layer. The H_w value is a parameter that has a strong impact on the bER since H_w is an exponential variable in Eq. (11). It may be necessary to increase the writing field sensitivity in the LC layer.

The damping constant α is only related to f_0, and so neither α nor time t are exponential variables in Eq. (11). Therefore, α and t are parameters with a weak impact on the bER as shown in Figs. 7 and 8, respectively.

There is a critical temperature, and information degradation will occur rapidly if this temperature is exceeded even for a short time as shown in Fig. 8.

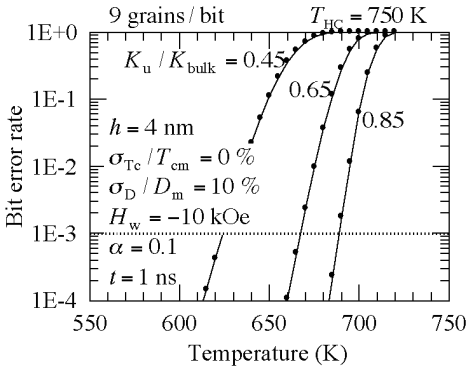

Fig. 9 Temperature dependence of bit error rate for various anisotropy constant ratios K_u/K_{bulk} (9 grains/bit).

Since increasing the grain number per bit is advantageous for increasing writing field sensitivity owing to a T_c variation problem[9], we consider a condition of 9 grains/bit as shown in Fig. 9 in addition to that of 4 grains/bit as shown in Fig. 1. A higher K_u/K_{bulk} > 0.85 than that for 4 grains/bit is preferable for the information stability at 650 K due to the smaller grain size when we take account of grain size and Curie temperature variations (see Fig. 10 (b)). Although a medium with K_u/K_{bulk} > 0.6 is difficult to manufacture, K_u/K_{bulk} must be increased in the HC layer.

In short, when a high K_u/K_{bulk} value can be achieved, the information in the HC layer appears to be stable up to about 650 K for T_{HC} of 750 K as shown in Fig. 10. At h of 4 nm, K_u/K_{bulk} values of about (a) 0.6 and (b) 0.85 are required for 4 and 9 grains/bit, respectively, taking account of certain variations, namely, a σ_{Tc}/T_{cm} of 2 % and a σ_D/D_m of 15 %.

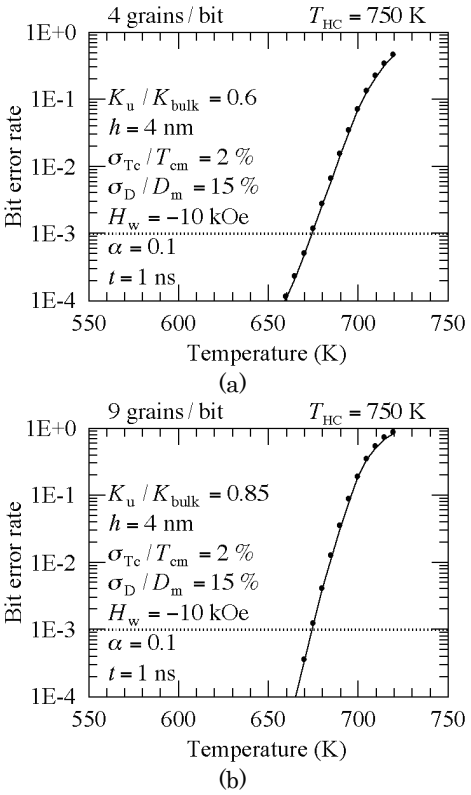

Fig. 10 Temperature dependence of bit error rate for (a) 4 and (b) 9grains/bit.

3.2 Determination of T_{HC} and T_{LC}

Next, we determine the Curie temperatures of T_{HC} and T_{LC}.

Figure 11 shows the temperature profile for the cross-track direction where T_{peak} is the peak temperature while writing in the LC layer, and D_T is the track width. The temperature was approximated using a linear profile with the thermal gradient $\partial T / \partial y$ for the cross-track direction.

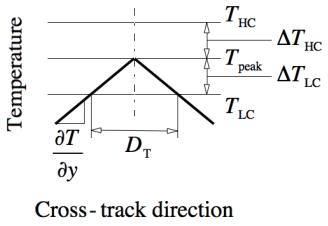

Fig. 11 Temperature profile for cross-track direction.

The temperature difference ΔT_{HC} between T_{HC} and T_{peak} is a function of the information stability in the HC layer while writing in the LC layer, and ΔT_{HC} was estimated to be about 100 K as discussed in 3.1.

The temperature difference ΔT_{LC} between T_{peak} and T_{LC} is a function of $\partial T / \partial y$ and D_T as

$$\Delta T_{LC} \approx \frac{\partial T}{\partial y} \cdot \frac{D_T}{2}. \qquad (12)$$

ΔT_{LC} was estimated to be about 100 K when using a $\partial T / \partial y$ of 10 K/nm and a D_T value of 20 nm.

Although a lower T_c, namely, a lower writing temperature, is better in terms of the heat resistance of the writing head and/or the surface lubricant, a higher K_u / K_{bulk} is required in a lower T_c medium for 10 years of archiving as described below in 3.3. And a medium with a high K_u / K_{bulk} is difficult to manufacture regardless of T_c. Therefore, we determined T_{HC} and T_{LC} values of 750 and 550 K, respectively, taking account of the results for ΔT_{HC} and ΔT_{LC}.

3.3 Information stability in HC and LC layers for 10 years of archiving

Finally, we discuss the information stability in the HC and LC layers for 10 years of archiving. We have already reported the information stability in HAMR for 10 years of archiving as regards h of 8 nm[3]. The calculation conditions are summarized in Table 2 taking account of certain variations, namely, a σ_{Tc} / T_{cm} of 2 % and a σ_D / D_m of 15 %. The storage temperature was 350 K. The maximum ambient temperature of a hard disk drive appears to be about 330 K. We take account of a certain margin of K_u / K_{bulk} for temperature since the bER increases rapidly as the temperature increases[3]. The K_u / K_{bulk} value was calculated for a bER of 1E - 3 under H_w = 0.

Table 2 Calculation conditions for 10 years of archiving in HC and LC layers.

Curie temperature T_{HC} (K)	750
Curie temperature T_{LC} (K)	550
Grain height h (nm)	4
Standard deviation of Curie temp. σ_{Tc} / T_{cm} (%)	2
Standard deviation of grain size σ_D / D_m (%)	15
Gilbert damping constant α	0.1
Storage time t (years)	10
Storage temperature T (K)	350
Signal threshold	0.5
Bit number (bits)	10^7
Allowable bit error rate	1E - 3

The required K_u / K_{bulk} values for the HC and LC layers are summarized in Table 3 for 10 years of archiving as are those for the HC layer while writing in the LC layer where h is 4 nm. High K_u / K_{bulk} values of 0.6 and 0.85 are necessary for the HC layer to realize the temperature difference ΔT_{HC} of 100 K needed for information stability while writing in the LC layer at 4 and 9 grains/bit, respectively. Although relatively low K_u / K_{bulk} values are required for the HC layer for 10 years of archiving, high K_u / K_{bulk} values of 0.64 and 1.29 are necessary for the LC layer due to its low T_c at 4 and 9 grains/bit, respectively. This can be explained using Fig. 12 in that the $K_u(350\,\mathrm{K})$ value for a

medium with a low T_c is intrinsically low when we compare the $K_u(350\ \mathrm{K})$ values for T_c = 750 and 550 K with the same K_u/K_{bulk} of 0.44. Therefore, a larger K_u/K_{bulk} of 1 is needed for a medium with a low T_c of 550 K if we are to obtain the same $K_u(350\ \mathrm{K})$ value as that for a medium with a high T_c of 750 K.

As shown in Table 3, the required K_u/K_{bulk} value at 9 grains/bit exceeds 1 for the LC layer. If h of 6 nm is realized, the required K_u/K_{bulk} value can be reduced from 1.29 to 0.86.

Table 3 Required K_u/K_{bulk} values for HC and LC layers in 3D HAMR.

h = 4 nm	HC layer	LC layer
4 grains/bit (D_m = 8.0 nm)		
Stability while writing in LC layer	> 0.6	
Stability for 10 years of archiving	> 0.28	> 0.64
9 grains/bit (D_m = 5.0 nm)		
Stability while writing in LC layer	> 0.85	
Stability for 10 years of archiving	> 0.56	> 1.29*

*0.86 (h = 6 nm)

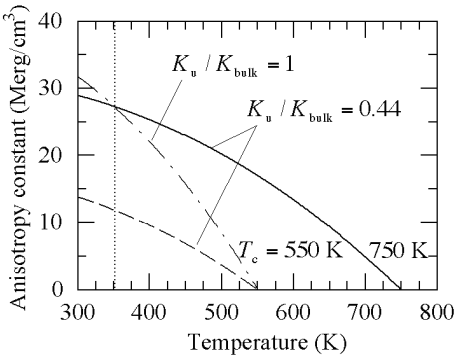

Fig. 12 Temperature dependence of anisotropy constant for Curie temperatures T_c of 750 (K_u/K_{bulk} = 0.44) and 550 K (K_u/K_{bulk} = 0.44 and 1).

4. Conclusions

We considered the information stability in a high Curie temperature T_{HC} (HC) layer while writing in a low Curie temperature T_{LC} (LC) layer, and the information stability in HC and LC layers for 10 years of archiving for three-dimensional heat-assisted magnetic recording (3D HAMR) at 2 Tbpsi (total density of 4 Tbpsi) employing an anisotropy constant ratio K_u/K_{bulk}.

The temperature difference ΔT_{HC} between T_{HC} and the peak temperature T_{peak} while writing in the LC layer is a function of the information stability in the HC layer, and it was estimated to be about 100 K for a grain height of 4 nm under a writing field of -10 kOe.

The temperature difference ΔT_{LC} between T_{peak} and T_{LC} is a function of the thermal gradient and the track width, and it was estimated to be about 100 K.

We determined T_{HC} and T_{LC} values of 750 and 550 K, respectively, taking account of the results for ΔT_{HC} and ΔT_{LC}.

A high K_u/K_{bulk} is necessary for the HC layer due to the information stability required while writing in the LC layer. A high K_u/K_{bulk} is also necessary for the LC layer when we consider 10 years of archiving since the anisotropy constant of an LC layer with a low T_{LC} is intrinsically low at the storage temperature due to its low Curie temperature. A medium with a high K_u/K_{bulk} must be manufactured if we are to realize 3D HAMR.

Acknowledgement We acknowledge the support of the Advanced Storage Research Consortium (ASRC), Japan.

References

1) S. H. Charap, P. -L. Lu, and Y. He: *IEEE Trans. Magn.*, **33**, 978 (1997).
2) T. Kobayashi, Y. Isowaki, and Y. Fujiwara: *J. Magn. Soc. Jpn.*, **39**, 8 (2015).
3) T. Kobayashi, Y. Nakatani, and Y. Fujiwara: *J. Magn. Soc. Jpn.*, **43**, 114 (2019).
4) T. Kobayashi, Y. Nakatani, and Y. Fujiwara: *J. Magn. Soc. Jpn.*, **42**, 110 (2018).
5) Western Digital: private communication.
6) E. D. Boerner and H. N. Bertram: *IEEE Trans. Magn.*, **34**, 1678 (1998).
7) M. Mansuripur and M. F. Ruane: *IEEE Trans. Magn.*, **MAG-22**, 33 (1986).
8) J. -U. Thiele, K. R. Coffey, M. F. Toney, J. A. Hedstrom, and A. J. Kellock: *J. Appl. Phys.*, **91**, 6595 (2002).
9) T. Kobayashi, Y. Nakatani, and Y. Fujiwara: *J. Magn. Soc. Jpn.*, **43**, 70 (2019).

Received Nov. 30, 2019; Accepted Jan. 16, 2020

J. Magn. Soc. Jpn., **44**, 40-44 (2020)

<Paper>

Micromagnetic Simulation of Voltage-Induced Spin Wave Resonance Properties in Ferromagnetic Nanowires with Perpendicular Anisotropy

X. Ya, R. Imai, T. Tanaka and K. Matsuyama

Faculty of Information Science and Electrical Engineering, Kyushu Univ., *Motooka 744, Nishi-ku, Fukuoka 819-0395, Japan*

A fundamental issue in developing spin wave (SW) devices with ultralow power consumption is exploring energy-efficient excitation with nanoscale spatial resolution. We numerically studied the voltage-induced excitation of a geometrically confined standing spin wave (SSW), which is suitable for the downsizing of various SW devices. The micromagnetic configuration of the excited SSW, the resonance spectrum, and the structural size effects were investigated. In addition, a possible application to a SSW-based logic operation was demonstrated in a nanowire with lateral dimensions of 20 nm × 100 nm.

Key words: spin wave, ferromagnetic resonance, magnetic anisotropy, micromagnetic simulation

1. Introduction

In solid-state physics, spin dynamics in magnetic nanostructures is an active research field[1-3]. In particular, the collective and coherent magnetization precession of spin waves (SWs) has attracted intense research interest[4,5]. The promising abilities of SWs have resulted in the novel research field of so-called magnonics[6-8], where the phase or amplitude of a propagating SW is used as a novel information carrier or a signal-processing medium. Energy-efficient excitation or manipulation of SWs is essential to exploit the potential ability of SW-based devices. Two different approaches to this problem, parametric pumping (PP)[1] and voltage-controlled magnetic anisotropy (VCMA)[9], have been intensively studied over the past years. PP is based on the nonlinear aspect of the spin dynamics, resulting in the excellent frequency-resolved excitation of short wavelength SWs, as experimentally observed in ferromagnetic oxide yttrium iron garnet[10-12] and metallic thin films[13-19]. Voltage-induced manipulations of magnetic properties have also been attracting intense research interest[20-24]. The superior performance of VCMA has been experimentally confirmed as being an ohmic dissipation free excitation of the ferromagnetic resonance[25-27], as opposed to conventional Oersted fields. In particular, the cooperative performance of PP and VCMA can be effectively exerted in a material system with perpendicular magnetic anisotropy[28]. Recently, the parametric excitation of propagating SWs via VCMA has been investigated using both theoretical[29] and numerical[30] approaches. However, the long distance propagation of SWs is still a challenging issue. In this study, the possibility of spatially resolved excitation of geometrically confined standing spin waves (SSWs) in magnetic nanostructures is addressed. A fundamental SW-based logic operation and its design considerations are also studied in the context of an application.

2. Numerical Model

Figure 1(a) shows a schematic figure of the investigated device structure, which consists of a perpendicularly magnetized nanowire and an overlaid gate electrode to apply electric fields for the local modulation of the perpendicular magnetic anisotropy (PMA). The following structural and magnetic parameters were adopted in the present study assuming ferromagnetic nanowires with interface-induced perpendicular anisotropy, such as the CoFeB/MgO system: the film thickness was t = 0.8 nm, the saturation magnetization was M_s = 1600 emu/cm^3, the exchange stiffness constant was A = 1.0 μerg/cm, the effective uniaxial perpendicular anisotropy field was H_k = 20 kOe, the gyromagnetic ratio was γ = 1.76 × 10^7 rad/s·Oe, and the Gilbert damping constant was α = 0.01. The electric field-induced modulation of the PMA was numerically modeled by the local sinusoidal H_k change using the amplitude of ΔH_k under the gate electrode. The assumed maximum value of ΔH_k (500 Oe) corresponds to an areal anisotropy energy change of 32.5 μJ/m^2, which is comparable to the experimentally reported values of several tens of μJ/m^2.[24,31,32] The dynamics of the SW caused by the electric field-induced PMA modulation was simulated by numerically integrating the Landau–Lifshitz–Gilbert equation. Subtle thermal agitation as a parallel PP seed was introduced via effective Langevin fields[33]. The Langevin fields with an amplitude based on fluctuation dissipation theorem and random orientation were applied to micromagnetic numerical cells at each time step[34]. The fourth-order Runge–Kutta method was adopted as a numerical scheme. The magnetization was assumed to be uniform along the film thickness and the wire width direction, taking into consideration that the dominant magnetization change was along the long axis of the nanowire. Therefore, the nanowire was discretized into a one-dimensional dipole array with a separation of 1 nm, and the dipole coupling was computed using an apparent surface charge model. A

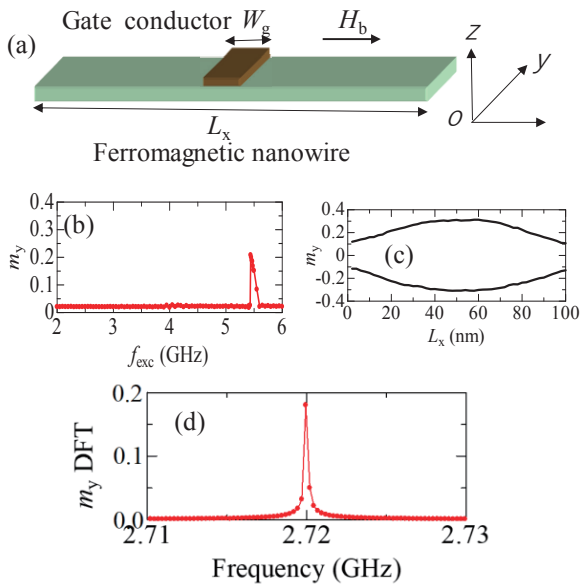

Fig. 1 (a) Schematic of a ferromagnetic nanowire with an overlaid gate electrode for SSW excitation, **(b)** dependence of the precession amplitude on the excitation frequency, **(c)** micromagnetic configuration of the SSW, and **(d)** the frequency spectra of the magnetization precession under the gate electrode.

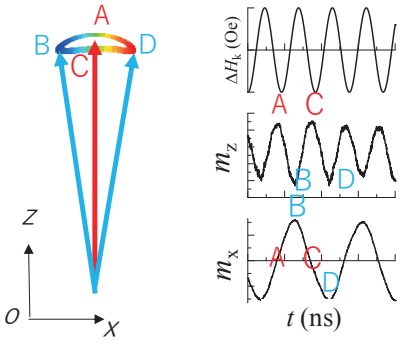

Fig. 2 Elliptic precession trajectory and phase relationship between the sinusoidal perpendicular anisotropy modulation and the magnetization components.

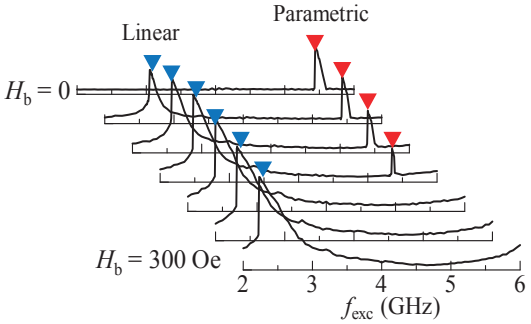

Fig. 3 SSW resonance properties at various external fields H_b applied along the long axis of the wire.

force-free boundary condition was assumed at the wire edge. The spatial discretization and the time step (10^{-15} s) were preliminarily optimized via the micromagnetic standard problem No. 4.[35]

3. Results and Discussion

Figure 1(b) presents the precession amplitude of the magnetization excited with a sinusoidal modulation of the perpendicular anisotropy field (ΔH_k = 500 Oe) under a gate electrode with a width of W_g = 10 nm, located at the center of a wire with lateral dimensions of 20 nm × 100 nm. The in-plane component of the normalized magnetization m_y at the wire center is plotted as a function of the excitation frequency, f_{exc}. The precession amplitude sharply decays below the resonance region (f_{exc} < 5.43 GHz) while gradually decreasing above the resonance region. The resonance frequency, f_{res} of 5.44 GHz, is twice the excited precession frequency, as shown in the frequency spectra of the magnetization precession (**Fig. 1(d)**), calculated from the digital Fourier transform of m_y. The micromagnetic configuration of the magnetization precession exhibits a first-order SSW along the long axis of the wire, as shown in **Fig. 1(c)**. These results confirm that the additional in-plane shape anisotropy of ferromagnetic wires with a nanoscale finite length causes an anisotropic precession trajectory accompanied by a time-varying m_z component with a frequency that is twice the precession frequency, which is essential as a seed for parallel parametric excitation. The results also reveal that the parametrically excited SSW exhibits an asymmetric resonance profile, similar to the case of a propagating SW[30]. The relative phase relationship between the time-varying PMA, m_x, and m_z indicates an apparent negative susceptibility, as shown in **Fig. 2**. That is, the increase in the perpendicular anisotropy field H_k leads to a decrease in m_z, and vice versa, reflecting the coherent SW resonance behavior.

The external bias field H_b applied along the long axis of the wire causes an additional linear mode excitation of the SSW, where the precession frequency is the same as the excitation frequency, as shown in **Fig. 3**. Conversely, the parametric mode disappears for H_b larger than 200 Oe. It can be reasoned that the precession axis is inclined to the x-axis due to the application of H_b, which results in the disappearance of the double period change in m_z necessary for a parallel parametric excitation seed. As can be seen in **Fig. 3**, the resonance profile of the parametric mode is markedly narrower than that of the linear mode, which would be suitable for frequency-selective SW-based device operations. **Figure 4** compares the dependence of the resonance precession amplitude m_y on the PMA modulation amplitude ΔH_k for the parametric and linear excitation modes at H_b = 100 Oe. m_y for the linear mode

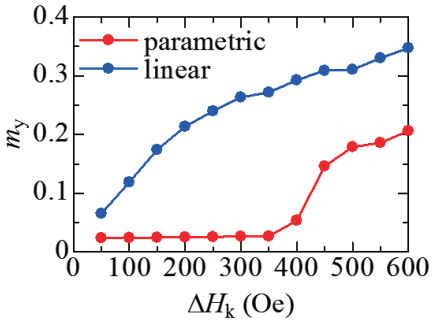

Fig. 4 SSW precession amplitude as a function of the sinusoidal anisotropy field amplitude ΔH_k for parametric and linear excitations.

linearly increases with increasing ΔH_k up to approximately 150 Oe and deviates from a linear response for larger ΔH_k. Conversely, the precession amplitude of the SSW in the parametric mode was found to be insensitive to the PMA modulation intensity for ΔH_k smaller than 350 Oe, resulting in mostly constant values of m_y due to the thermal disturbance. The observed threshold for triggering the parallel parametric excitation has been theoretically predicted for a propagating SW[29,30].

The dependences of the parametric excitation properties on representative structural parameters are presented in **Figs. 5** and **6**. **Figure 5(a)** compares the resonance profile of SSWs excited in wires with various wire lengths L_x and a fixed gate electrode width (W_g =

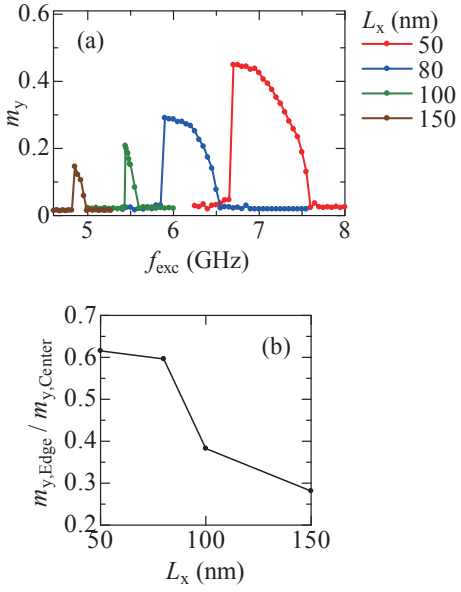

Fig. 5 Dependence of the SSW properties on the wire length L_x: **(a)** the resonance spectra and **(b)** the nonuniformity of the precession amplitude along the wire.

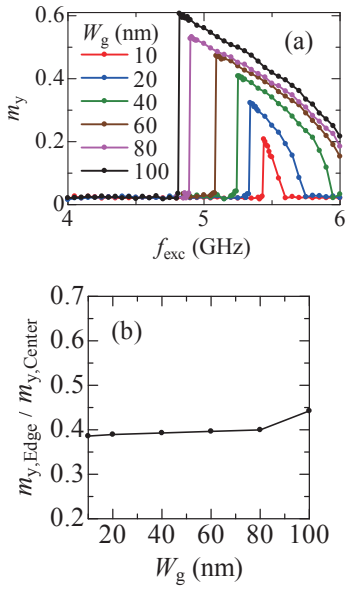

Fig. 6 Dependence of the SSW properties on the gate electrode width wire length W_g: (a) the resonance spectra and (b) the nonuniformity of the precession amplitude along the wire.

10 nm). The values of f_{opt}, at which the precession amplitude reaches its maximum value, increase from 4.8 GHz to 6.7 GHz with L_x decreasing from 150 nm to 50 nm, reflecting the dispersion relation between the SW length and the excitation frequency. The observed broad spectrum in the short length wire can be associated with the large amplitude precession, geometrically confined in the narrow region; m_y = 0.45 (L_x = 50 nm), m_y = 0.16 (L_x = 150 nm). **Figure 5(b)** shows the relative ratio of the precession amplitude at the center ($m_{y,center}$) and edge ($m_{y,edge}$) of the wire. The variation of the precession amplitude along the wire axis markedly decreases with decreasing L_x and closes to the ferromagnetic resonance mode.

Even though f_{opt} and the nonuniformity of the precession amplitude also depend on the gate electrode width W_g, as shown in **Fig. 6(a), (b)**, this dependency is relatively weak compared to that on the wire length. That is, the increase in the values of W_g, which ranged from 10 nm to 100 nm, resulted in 15% and 18% increases in f_{opt} and $m_{y,edge}/m_{y,center}$, respectively. **Figure 6(a)** shows that the precession amplitude monotonously increases with increasing W_g. These results indicate a spatial integration effect in the voltage-induced excitation of the SSW, which can be applied to a logic operation as follows.

Figure 7(b) presents the frequency spectra of the precession amplitude excited with two electrodes located 25 nm and 75 nm from the wire end (**Fig. 7(a)**). The values of L_x and W_g were chosen to be 100 nm and 10 nm, respectively. A bias field of 100 Oe was applied along the wire axis. The two plots show the results for the different phase differences $\Delta\phi$ (=0, π) between the sinusoidal anisotropy changes in the two electrodes.

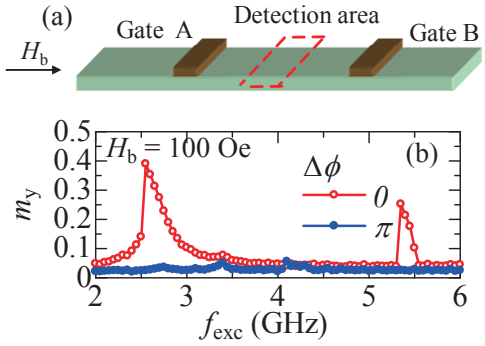

Fig. 7 (a) Schematic of two-generator device. **(b)** Comparison of the frequency spectra between the in-phase ($\Delta\phi$ = 0) and opposite-phase ($\Delta\phi$ = π) excitations with two electrodes located along the wire.

Two resonance peaks similar to those excited with one electrode are observed in the in-phase excitation ($\Delta\phi$ = 0). Conversely, no distinguished excitation of the SSW was caused by the opposite-phase excitation ($\Delta\phi$ = π). This result indicates that opposite PMA changes at different positions cancel out through the wire for both of the linear and parametric mode excitations, which can be used as phases comparing microwave voltages

Another example of spatial integration of the voltage-induced SSW excitation with two electrodes is demonstrated in **Fig. 8**. The same device structure, as that shown in **Fig. 7**, was assumed. When an in-phase PMA modulation with f_{exc} = 5.44 GHz was applied with two electrodes (G_A:1, G_B:1), a parametric SSW was excited with ΔH_k larger than 200 Oe. A micromagnetic configuration of the SSW excited with two electrodes is shown in **Fig. 8(b)**. Conversely, an SSW was not formed with a single-electrode excitation (G_A:0, G_B:1), even when ΔH_k was larger than twice the excitation threshold for the two-electrode excitation. Note that the precession amplitude for the single-electrode excitation was suppressed within the thermal noise level due to the existence of a threshold on the parallel parametric excitation. These results should be applicable to the AND gate operation for nanostructured SW logic devices. Noise floor for the ΔH_k lower than 200 Oe (G_A:1, G_B:1) was somewhat smaller than that shown in **Fig.7** ($\Delta\phi$ = 0), since the higher ΔH_k of 500 Oe was assumed in the spectra simulations of **Fig. 7**. The noise level of the single-electrode excitation also exhibits smaller value independent on the value of ΔH_k.

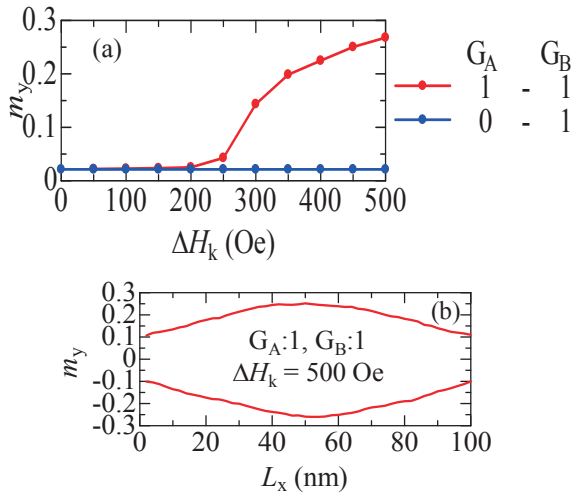

Fig. 8 (a) Comparison between the SSW precession amplitude for the one-gate (G_A:0, G_B:1) and simultaneous two-gate (G_A:1, G_B:1) excitations. **(b)** Micromagnetic configuration of the SSW excited with two electrodes.

4. Conclusions

The voltage-induced excitation of geometrically confined SSWs in nanowires with perpendicular anisotropy was numerically studied via micromagnetic simulations. Sinusoidal modulations of perpendicular anisotropy fields were found to cause linear and parametric mode excitations of SSWs depending on the external field. The dependence of the SSW resonance properties on the structural parameters was systematically examined. A possible application to a SSW-based logic operation was demonstrated in a nanowire with lateral dimensions of 20 nm × 100 nm, where the spatial integration effect of the voltage-induced anisotropy modulation was used.

Acknowledgements This study has been partly supported by the Japan Society for the Promotion of Science (JSPS) KAKENHI under Grand-in-aid Number JP17J09702.

References

1) B. Hillebrands and K. Ounadjela, "Spin dynacs in confined magnetic structutrees 1", *Springer* (2001).
2) G. Bertotti, I. Mayergoyz and C. Serpico, "Nonlinear magnetization dynamics in nanosystems", *Ersevier*, (2009).
3) H. Zabel and M. Farle (Eds), "Magnetic Nanostructures", *Springer Tracts in Modern Physics*, 246 (2013).
4) A. G. Gurevich and G. A. Melkov, "Magnetization oscillations and waves", *CRC Press* (1996).
5) D. D. Stancil and A. Prabhakar, "Spin waves", *Springer* (2009).
6) V. V. Kruglyyak, S. O. Demokritov and D. Grundler, "Magnonics", *J. Phys. D: Appl. Phys.***43**, 264001 (2010).
7) B. Lenk, H. Ulrichs, F. Garbs and M. Munzenberg, *Physics Reports*, **507**, 107 (2011).
8) A. V. Chumak, V. I. Vasyuchka, A. A. Serga and B. Hillebrands, *Nature Phys.*, **11**, 453 (2015).
9) F. Matsukura, Y. Tokura and H. Ohno, *Nature Nanotech.* **10**, 209 (2015).
10) H. Kurebayashi, O. Dzyapko, V. E. Demidov, D. Fang, A. J. Ferguson and S. O. Demokritov, *Appl. Phys. Lett.*, **99**, 162502 (2011).
11) C. W. Sandweg, Y. Kajiwara, A. V. Chumak, A. A. Serga, V. I. Vasyuchka, M. B. Jungfleisch, E. Saitoh and B. Hillebrands, *Phys. Rev. Latt.*, **106**, 216601 (2011).

12) A. A. Serga, C. W. Sandweg, V. I. Vasyuchka, M. B. Jungfleish, B. Hillebrands, A. Kreisel, P. Kopietz and M. P. Kostylev, *Phys. Rev.* **B 86**, 134403 (2012).
13) G. A. Melkov, Yu. V. Koblyanskiy, R. A. Slipets, A. V. Talalaevskij and A. N. Slavin, *Phys. Rev.* **B 79**, 134411 (2009).
14) S. Urazhdin, V. Tiberkevich and A. Slavin, *Phys. Rev. Lett.*, **105**, 237204 (2010).
15) H. Ulrichs, V. E. Demidov, S. Demokritov and S. Urazhdin, *Phys. Rev.* **B 84**, 094401 (2011).
16) T. Bracher, P. Pirro, B. Obry, B. Leven, A. A. Serga and B. Hillebrands, *Appl, Phys. Lett.*, **99**, 162501 (2011).
17) T. Bracher, P. Pirro, A. A. Serga and B. Hillebrands, *Appl. Phys. Lett.*, **103**, 142415 (2013).
18) T. Bracher, P. Pirro, F. Heussner, A. A. Serga and B. Hillebrands, *Appl. Phys. Lett.*, **104**, 092418 (2014).
19) A. Capua, C. Rettner and S. Parkin, *Phys. Rev. Lett.*, **116**, 0247204 (2016).
20) M. Weisheit, S. Fähler, A. Marty, Y. Souche, C. Poinsignon and D. Givord, *Science* **315**, 349 (2007).
21) C-G Duan, J. P. Velev, R. F. Sabirianov, Z. Zhu, J. Chu, S. S. Jaswal and E. Y. Tsymbal, *Phys. Rev. Ret.* **101**, 137201 (2008).
22) D. Chiba, M. Sawicki, Y. Nishitani, Y. Nakatani, F. Matsukura and H. Ohno, *Nature* **455**, 515 (2008).
23) M. Tsujikawa and T. Oda, Phys. *Rev. Lett.,* **102**, 247203 (2009).
24) T. Nozaki, Y. Shiota, M. Shiraishi, T. Shinjo and Y. Suzuki, *Appl. Phys. Lett.*, **96**, 022506 (2010).
25) T. Nozaki, Y. Shiota, S. Miwa, S. Murakami, F. Bonell, S. Ishibashi, H. Kubota, K. Yakushiji, T. Saruya, A. Fukushima, S. Yuasa, T. Shinjo and Y. Suzuki, N*ature Phys.* **8**, 491 (2012).
26) S. Kanai, M. Gajek, D. C. Worledge, F. Matsukura and H. Ohno, "Electric field-induced ferromagnetic resonance in a CoFeB/MgO magnetic tunnel junction under dc bias voltages", *Appl Phys. Lett.* **195**, 242409 (2014).
27) K. Miura, S. Yabuuchi, M. Yamada, M. Ichimura, B. Rana, S. Ogawa H. Takahashi, Y. Fukuma, Y. Otani, "Voltage-induced magnetization dynamics in CoFeB/MgO/CoFeB magnetic tunnel junctions", *Scientific Reports* **7**, 42511 (2017).
28) Y-J. Chen, H. K. Lee, R. Verba, J. A. Katine, I. Barsukov, V. Tiberkevich, J. Q. Xiao, A. N. Slavin and I. N. Krivorotov, "Parametric Resonance of Magnetization Excited by Electric Field", *Nano Lett.* **17**, 572 (2017).
29) R. Verba, V. Tiberkevich, I. Krivorotov and Andrei Slavin, *Phys. Rev. Appl.* **1**, 044006 (2014).
30) R. Verba, M. Carpentieri, G. Finocchio, V. Tiberkevich and A. Slavin, *Scientific Reports* **6**, 25018 (2016),
31) Y. Shiota, F. Bonell, S. Miwa, N. Mizuochi, T. Shinjo and Yoshishige Suzuki, *Appl. Phys. Lett.*, **103**, 082410 (2013).
32) Y. Shiota, T. Nozaki, S. Tamaru, K. Yakushiji, H. Kubota, A. Fukushima, S. Yuasa and Y. Suzuki, Appl. Phys. Lett., 111, 022408 (2017).
33) W. F. Brown, *Phys. Rev*, **130**, 1677 (1963).
34) O. Chubykalo, J. D. Hannay, M. Wongsam, R. W. Chantrell and J. M. Gonzalez, *Phys. Rev.* **B. 65**, 184428 (2002).
35) V. D. Tsiantos, D. Suess, T. Schrefl and J. Fidler, *J. Appl. Phys.*, **89**, 7600 (2001).

Received Oct. 08, 2019; Accepted Jan. 07. 2020

J. Magn. Soc. Jpn., **44**, 45-51 (2020)

<Paper>

Study on Asymmetric Magnetic Pole Structure for IPM Motor Using Neodymium Bonded Magnet

T. Yanagisawa, Y. Yoshida*, and K. Tajima

Department of Cooperative Major in Life Cycle Design Engineering, Akita Univ., *1-1, Tegata Gakuen-machi, Akita 010-8502, Japan*

*Department of Mathematical Science and Electrical-Electronic-Computer Engineering, Akita Univ., *1-1, Tegata Gakuen-machi, Akita 010-8502, Japan*

In this paper, we propose an interior permanent magnet synchronous motor (IPMSM) with an asymmetric magnetic pole structure that uses bonded neodymium magnets. By adopting the asymmetrical magnet arrangement, the current phase angle, where the magnetic torque is maximized, can be set to almost the same phase while maximizing the reluctance torque. To verify the usefulness of the proposed motor, we prototyped an actual motor on the basis of our proposed motor and compared the characteristics with a conventional IPMSM that uses sintered neodymium magnets. Although the torque of the proposed motor was smaller than the conventional motor due to a problem with the dimensions of the bonded neodymium magnets, it was shown that an IPMSM with an asymmetrical magnetic pole structure that uses Dy-free bonded neodymium magnets can achieve performance equivalent to conventional IPMSMs that use sintered neodymium magnets.

Keywords: permanent magnet synchronous motor, interior permanent magnet synchronous motor, neodymium bonded magnet, asymmetric pole structure, heavy rare earth free

1. Introduction

In recent years, interest in protecting the global environment and conserving energy has been growing. Among electric motors, permanent magnet synchronous motors (IPMSMs) using high-performance rare earth magnets for high-efficiency motors have been applied to various fields. Neodymium (Nd) and dysprosium (Dy) are key elements for improving the performance of PMSMs; however, the production of Dy, a heavy rare-earth element, depends on specific countries. Therefore, developing high-efficiency motors without using Dy is required.

Although neodymium bonded magnets have a lower residual magnetic flux density than neodymium sintered magnets, they are expected to be applied to motors as Dy-free magnets because of their advantages, such as a stronger residual magnetic flux density than ferrite magnets, high degree of freedom in terms of shape, and zero generation of eddy currents.

Since IPMSMs can utilize reluctance torque in addition to magnetic torque, a higher torque can be expected compared with PMSMs that do not utilize reluctance torque. Although it has been reported that reluctance torque is used to achieve the same output characteristics, power density, and efficiency characteristics as rare earth magnets even when ferrite magnets are used[1], it is difficult to produce a torque density equivalent to that of a rare earth magnet motor only with a ferrite magnet. In examining the optimum shape of an IPMSM using a rare-earth bonded magnet, a torque equivalent to that of rare earth sintered magnet IPMSMs has been realized, but the rotor has an overhang structure, and there are still problems with further downsizing these IPMSMs[2].

Generally, an IPMSM has a phase difference of 45 degrees between the current phase angle at which the magnetic torque is maximized and the current phase angle at which the reluctance torque is maximized. Therefore, there has been study on improving the total torque by arranging the magnets asymmetrically and shifting the phase of the magnetic torque[3)-6)]. In asymmetric rotor designs for the permanent magnet-assisted synchronous reluctance motor, the total torque was increased by designing the rotor to have an asymmetric structure, but the reluctance torque was reduced compared with the conventional structure[4),6)].

In this study, we design and prototype an asymmetric pole rotor for an IPM motor with improved reluctance torque compared with the previous model studied[7)].

2. Principle of improving torque with asymmetric pole structure

Here, we use a 2-pole inset-type PMSM rotor having saliency to explain the principle of improving the torque with the asymmetric pole structure. Fig. 1 (a) and (b) show the torque generation principle of an inset-type PMSM. The center of the north pole of the magnet is the d-axis, and the direction advanced 90 degrees from the d-axis in the rotational direction is the q-axis. The magnetic torque generated by suction and repulsion forces acting between the pole of the rotating magnetic field and the pole of the permanent magnet placed on the rotor is maximized by the magnetic field rotating in the q-axis direction as shown in Fig. 1 (a). The reluctance torque that is generated by the suction force acting between the salient pole of the rotor and the rotating magnetic field is maximized by the magnetic field rotating in the direction advanced 45 degrees from the q-axis as shown in Fig. 1 (b). Therefore, the maximum value of both torque components cannot be generated simultaneously.

To generate the maximum value of these two

torque components simultaneously, the phase of the magnets is advanced without changing the phase of the rotor saliency shown as Fig. 2. In Fig. 2, the magnets are divided and arranged in a phase-shifted manner, while the phase of the rotor saliency remains the same as the conventional inset-type PMSM as shown in Fig. 1 (a). If the phase shift of the magnet poles can be advanced 45 degrees from the q-axis direction, the maximum torque of the two components can be generated at the same phase, and the total torque can be improved.

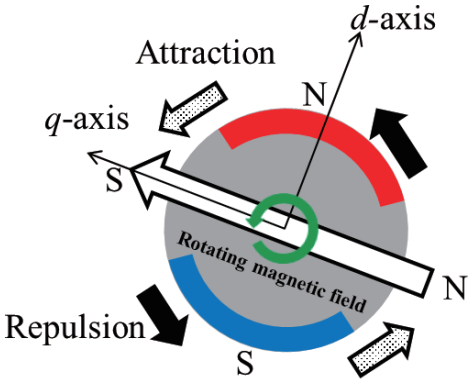

(a) Magnetic torque

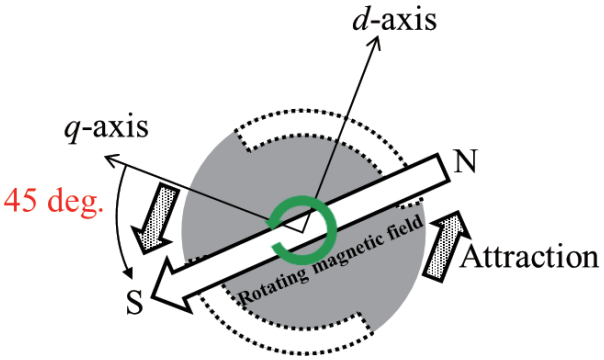

(b) Reluctance torque

Fig. 1. Principle of torque generation of 2-pole inset-type PMSM

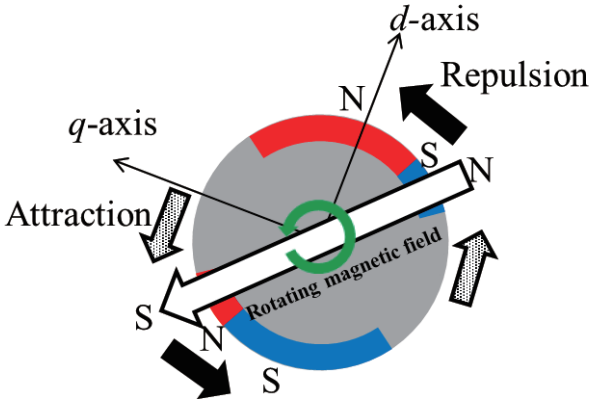

Fig. 2. Principle of magnetic torque generation when magnets are divided and arranged in phase-shifted manner

3. Analysis of examined motors

3.1 Overview of examined motors

Fig. 3 (a) shows the conventional IPMSM with 4-pole sintered neodymium magnets (base model), and Fig. 3 (b) shows the proposed IPMSM with a 4-pole asymmetric rotor structure using bonded neodymium magnets. The stator is common to both models. Table 1 shows the motor specifications. The residual magnetic flux density of the sintered neodymium magnets used in the base model and bonded neodymium magnets used in the proposed model are 1.27 T and 0.71 T, respectively.

Fig. 4 (a) and (b) show the rotor shapes and magnetization directions of the base and proposed models. The void arrows in the figure indicate the magnetization direction of the magnet. The part highlighted on the rotor surface with the solid line represents the N pole, and that highlighted with the broken line represents the S pole. The magnetization direction of the base model faces the same direction as the d-axis direction. In the rotor of the proposed model, since the magnets are arranged asymmetrically, the magnetic pole center exists at a position shifted from the d-axis direction.

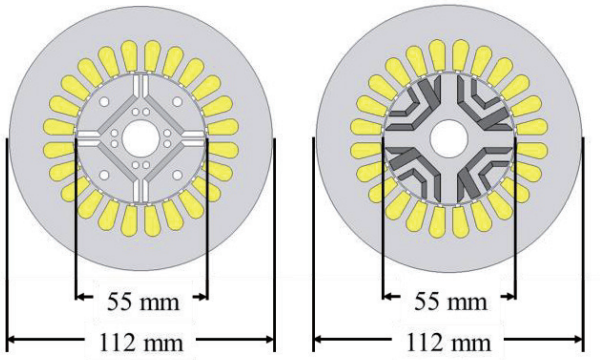

(a) Base model (b) Proposed model

Fig. 3. Shape of motors under consideration

Table1 Specifications of analytical models

Parameter	Base	Proposed
Permanent magnet material	Neodymium sintered	Neodymium bonded
Core material	50A350	
Coil	Copper	
Stator outer diameter (mm)	112	
Rotor outer diameter (mm)	55	
Gap width (mm)	0.5	
Stack length (mm)	30	
Number of winding turns/slot	35	
Number of slots	24	
Number of poles	4	
Residual flux density B_r (T)	1.27	0.71
Coercive force H_c (kA/m)	876	470
Recoil permeability μ_r	1.05	1.20

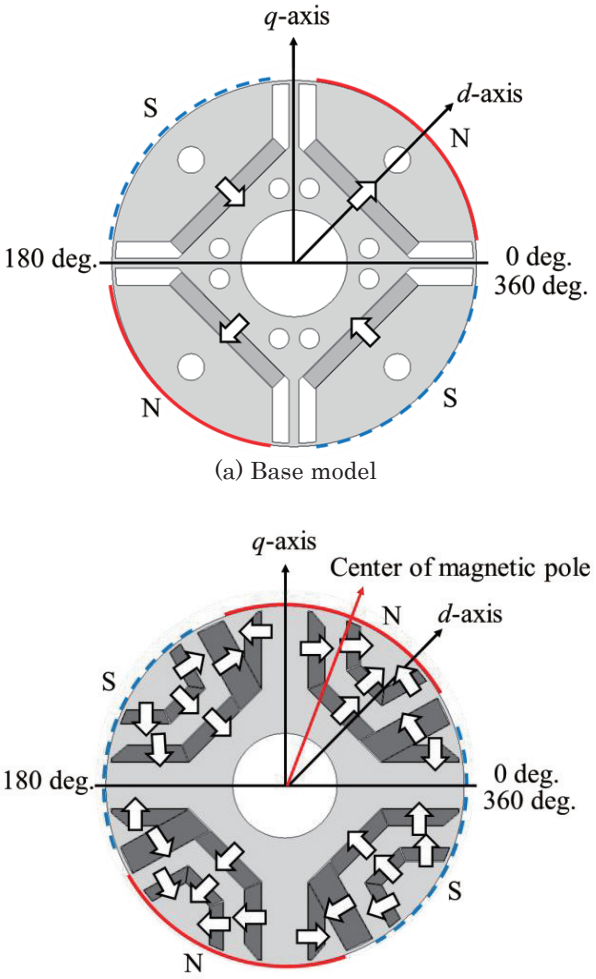

(a) Base model

(b) Proposed model

Fig. 4. Magnetization direction

3.2 Comparison of torque characteristics

Fig. 5 shows the torque characteristics of the examined motors. The magnetic torque is indicated by the broken line, and the reluctance torque is indicated by the dotted line. The solid line is the total torque, that is, the sum of the magnetic torque and reluctance torque. The maximum magnetic torque of the base model was 0.85 N·m when the current phase angle β was 0 degrees, and the maximum value of the reluctance torque was 0.20 N·m when the current phase angle β was 45 and −135 degrees. The maximum magnetic torque of the proposed model was 0.77 N·m when the current phase angle β was 40 degrees, and the maximum reluctance torque was 0.18 N·m when the current phase angle β was 50 and −140 degrees. Therefore, the phase of the magnetic torque of the proposed model was shifted by 40 degrees compared with the base model, and it was confirmed that the current phases at which the magnetic and reluctance torques were maximum were almost the same. Comparing the maximum values of the total torque, the base model was 0.92 N·m when the current phase angle β was 20 degrees, and that of the proposed model was 0.94 N·m when the current phase angle β was 45 degrees. The proposed model obtained a maximum total torque equivalent to the base model when the phase of the magnetic torque was shifted by 40 degrees.

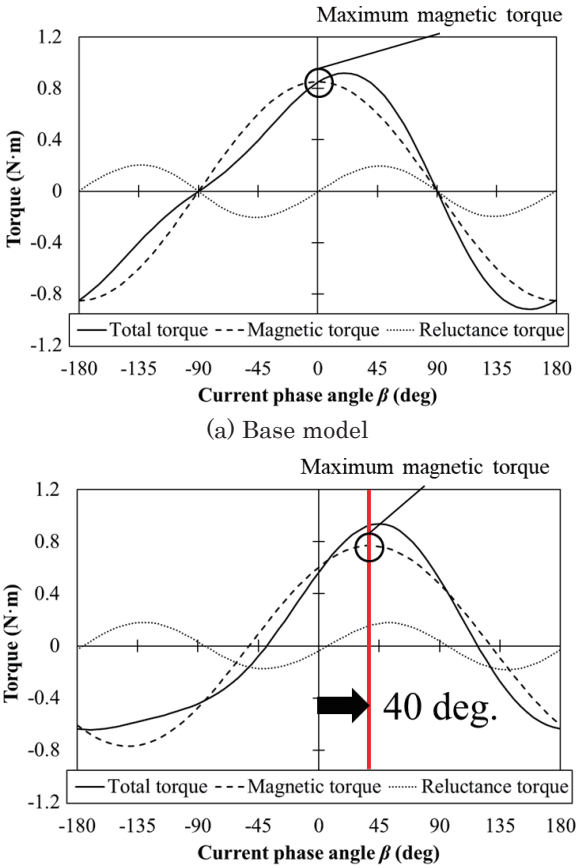

(a) Base model

(b) Proposed model

Fig. 5. Torque characteristics of examined motors

4. Experimental verification of motor performance

4.1 Experimental setup

Fig. 6 shows photographs of a prototype stator and rotors used in an experiment. The same stator was used to measure the characteristics of the two motors. Fig. 7 shows a photograph of the experimental apparatus. The waveform of back electromotive force (EMF) was recorded by using a memory high coder. The input electric power of the motor P_{in} was measured by using a power meter connected just before the motor, and the mechanical output power of the motor P_{out} was obtained from the product of the average torque T and the rotational angular velocity ω measured by the torque detector shown in the figure.

4.2 Comparison of calculated and measured values

Fig. 8 (a) shows the back EMF waveform of the base model at 1300 rpm, and Fig. 8 (b) shows that of the proposed model. In the figures, the measured and calculated values are compared with each other.

The fundamental wave component was extracted from these waveforms with a fast Fourier transform (FFT) The relationship between the rotational speed and the fundamental component of the back EMF is shown in Fig. 9; Fig. 9 (a) is the base model, and Fig. 9 (b) is the proposed model. Comparing the calculated and measured values at 1300 rpm, the experimental value of the base model was 6.17% smaller than the calculated value, and the experimental value of the

proposed model was 17.9% smaller than the calculated value. The reason for the larger error for the proposed model is that there were gaps between the magnet and the iron core greater than the designed value because of variation in the prototype magnet dimensions.

(a) Common stator

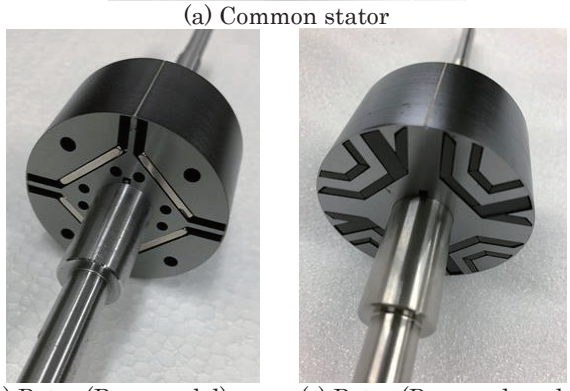

(b) Rotor (Base model) (c) Rotor (Proposed model)

Fig. 6. Actual machines

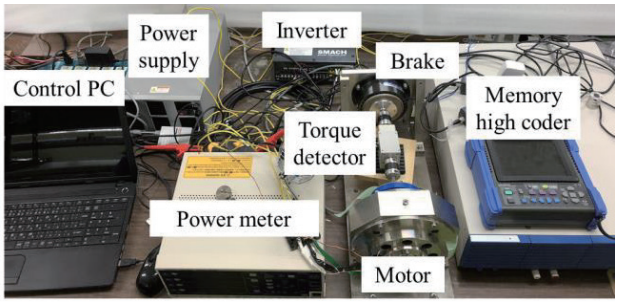

Fig. 7. Experimental apparatus

Fig. 10 shows the relationship between the current amplitude and torque of the base and proposed models at rotation speeds of 500, 1000, and 1300 rpm. The calculated values are indicated by the solid lines, and the measured values are indicated by the symbols. The current amplitude used for the horizontal axis of the graphs was the fundamental wave amplitude extracted by FFT from a current waveform including harmonic components as shown in Fig. 11. The current phase was selected so that the output torque was maximized for each current amplitude. From Fig. 10, the calculated value of the torque of the base model almost agreed with the experimental value at all rotational speeds, while the calculated value of the proposed model was larger than the experimental value. These results also

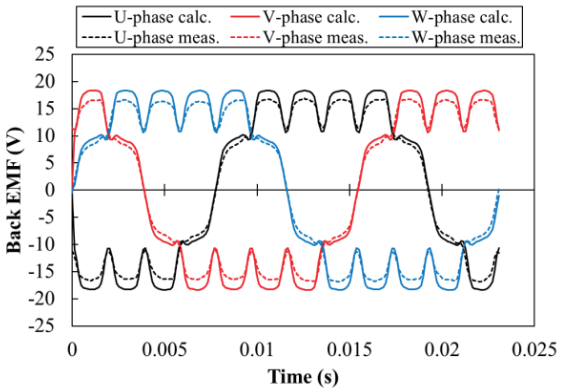

(a) Base model

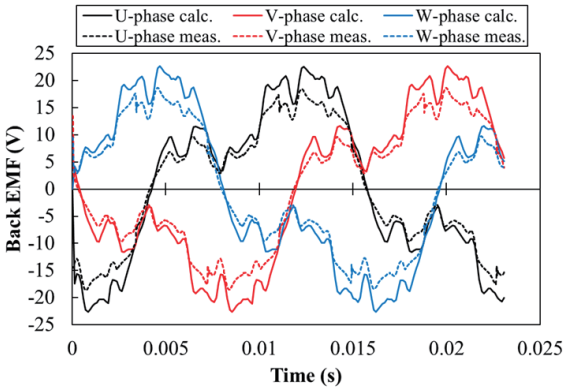

(b) Proposed model

Fig. 8. Back EMF waveform at 1300 rpm

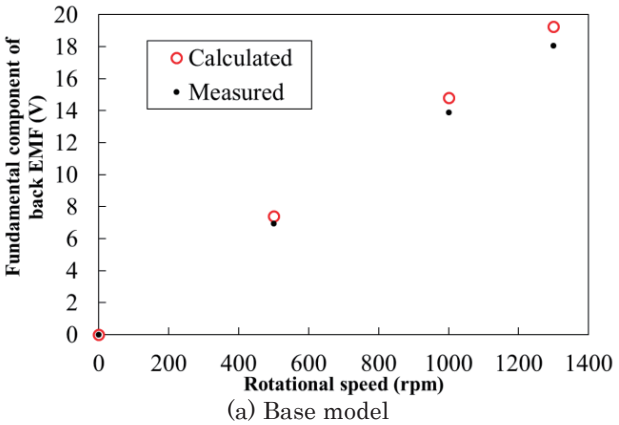

(a) Base model

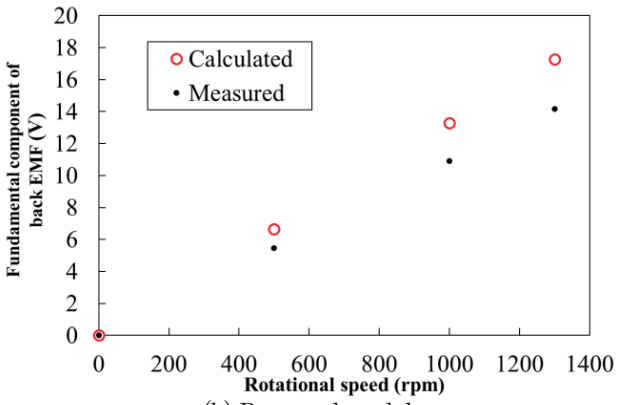

(b) Proposed model

Fig. 9. Relationship between rotational speed and fundamental component of back EMF.

show that the proposed model could not be prototyped as designed due to variation in the magnet dimensions. It was shown that an asymmetrical magnetic pole structure for an IPMSM using Dy-free bonded neodymium magnets could achieve performance equivalent to the conventional IPMSM using sintered neodymium magnets if we can eliminate the error of the dimensions.

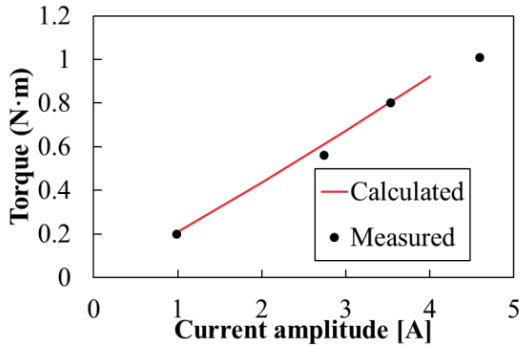

(a) Base model at rotational speed of 500 rpm

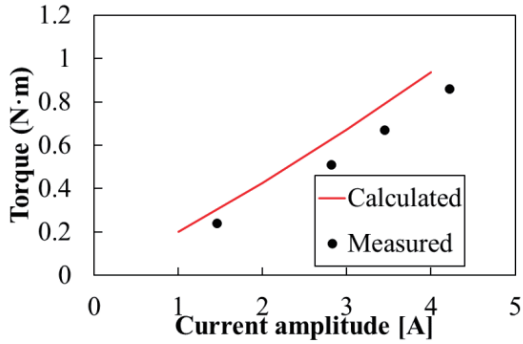

(b) Proposed model at rotational speed of 500 rpm

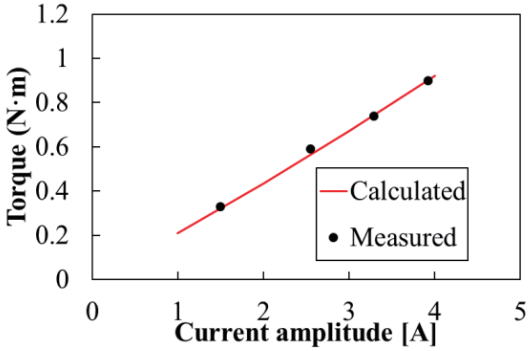

(c) Base model at rotational speed of 1000 rpm

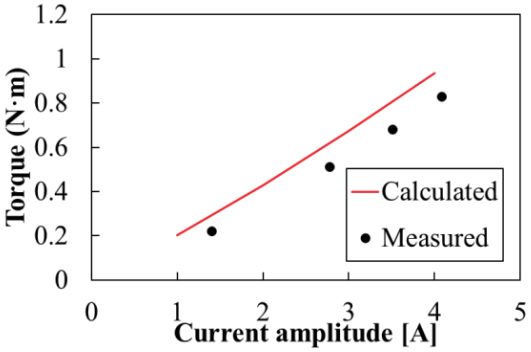

(d) Proposed model at rotational speed of 1000 rpm

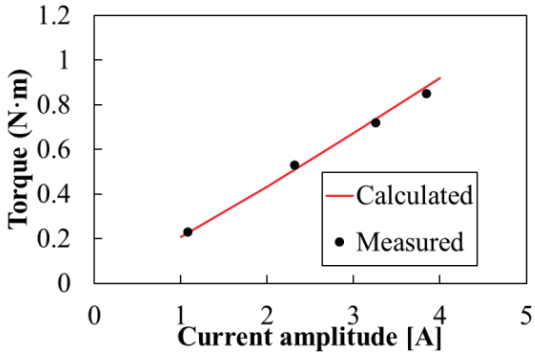

(e) Base model at rotational speed of 1300 rpm

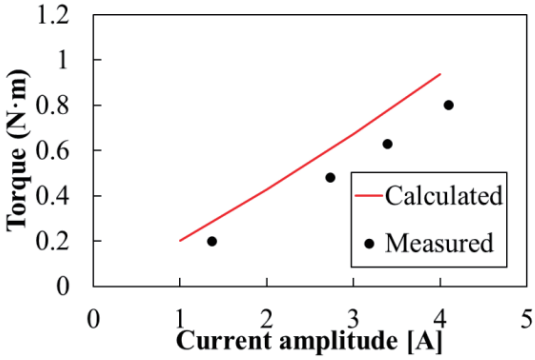

(f) Proposed model at rotational speed of 1300 rpm.

Fig. 10. Relationship between current amplitude and torque

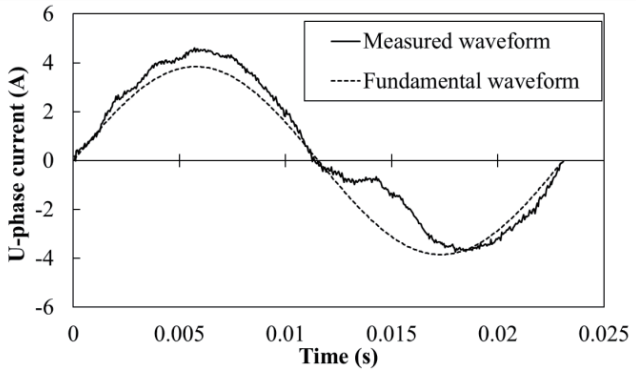

(a) Base model

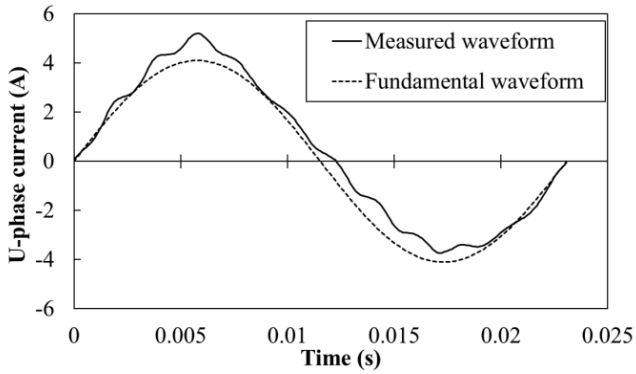

(b) Proposed model

Fig. 11. U-phase current waveform at maximum torque at 1300 rpm

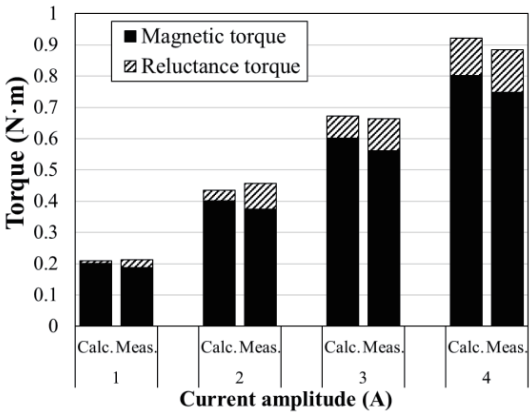

(a) Base model

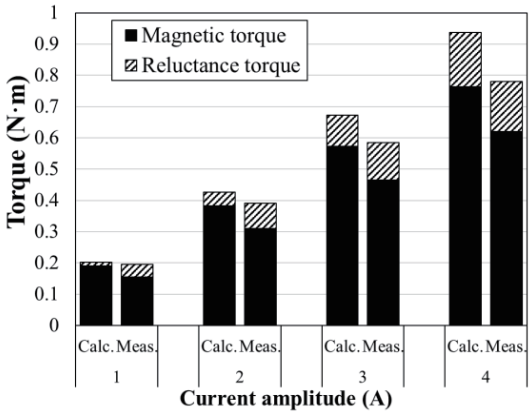

(b) Proposed model

Fig. 12. Relationship between current amplitude and separated torque components at 1300 rpm

Fig. 12 shows the relationship between current amplitude and separated torque components at 1300 rpm. The components were separated by using the following equations.

$$\Psi_a = \frac{V_0}{\omega} \tag{1}$$

$$T_m = P_n \Psi_a i_q \tag{2}$$

$$T_r = T - T_m \tag{3}$$

Here, V_0, ω, P_n, Ψ_a, i_q, T_m, T_r, and T are values converted by the d-q transformation of the back EMF, angular velocity, number of pole pairs, magnetic flux of magnets, q-axis current, magnetic torque, reluctance torque, and total torque obtained in the experiments and calculation. The magnetic torque was calculated by multiplying Ψ_a, P_n and i_q. The reluctance torque was calculated by subtracting T_m from T.

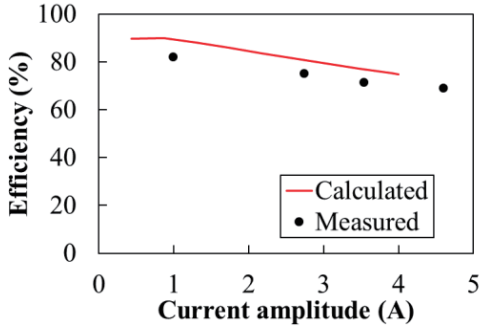

(a) Base model at rotational speed of 500 rpm

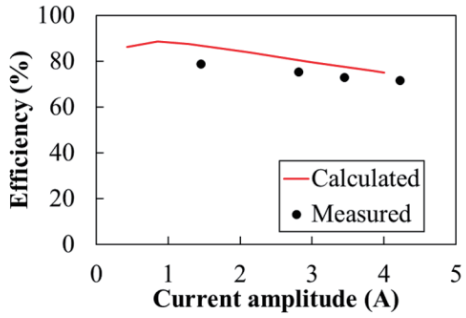

(b) Proposed model at rotational speed of 500 rpm

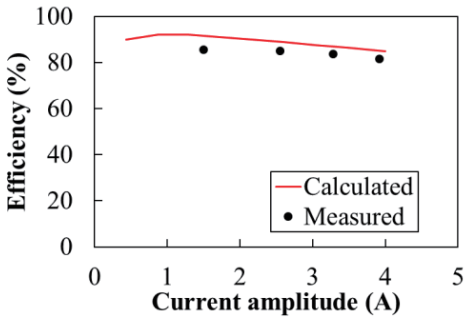

(c) Base model at rotational speed of 1000 rpm

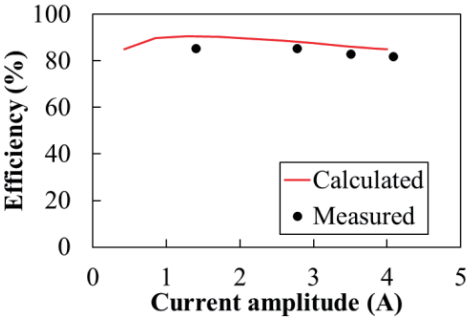

(d) Proposed model at rotational speed of 1000 rpm

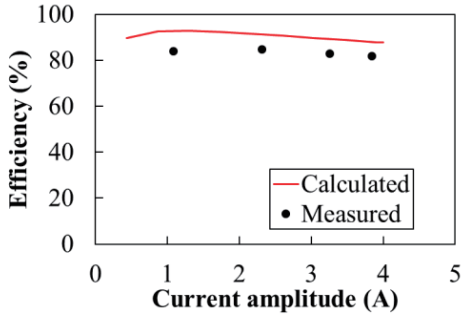

(e) Base model at rotational speed of 1300 rpm

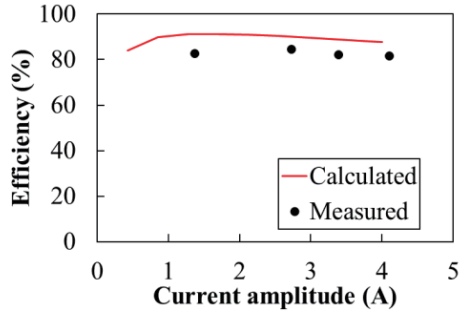

(f) Proposed model at rotational speed of 1300 rpm

Fig. 13. Relationship between current amplitude and efficiency

The magnetic torque is indicated by the filled bars, and the reluctance torque is indicated by the hatched bars. It can be seen from this figure that the experimental value of the proposed model's magnetic torque is lower than the calculated value.

Fig. 13 shows the relationship between the current amplitude and the efficiency of the base and proposed models at rotation speeds of 500, 1000, and 1300 rpm. The calculated values are indicated by the solid lines, and the experimental values are indicated by the symbols. In the figures, the experimental values of efficiency were smaller than the calculated ones at all rotational speeds because the effect of the increase in iron loss due to harmonics and mechanical loss were not considered for the calculated values. The maximum efficiency of the measured values was 85.6% for the base model and 85.4% for the proposed model; the maximum efficiency of both models had almost the same value.

5. Conclusion

In this paper, we proposed an asymmetrical magnetic pole structure for an IPMSM using bonded neodymium magnets. We prototyped the proposed motor and compared the characteristics with a conventional IPMSM using sintered neodymium magnets. By adopting the asymmetrical magnet arrangement, the current phase angle, where the magnetic torque is maximized, could be set to almost the same phase by maximizing the reluctance torque.

Although the torque of the proposed motor was smaller than the conventional motor due to a problem with the dimensions of the bonded neodymium magnets, it was shown that this asymmetrical magnetic pole structure for IPMSMs using Dy-free bonded neodymium magnets could achieve performance equivalent to the conventional IPMSM using sintered neodymium magnets.

As future work, we plan to simplify the shapes of the magnets to prevent dimensional errors.

References

1) M. Sanada, Y. Inoue, and S. Morimoto: *IEEJ Trans. on IA*, **13**, 1401 (2011).
2) Y. Yoshikawa, T. Ogawa, Y. Okada, S. Tsutsumi, H. Murakami, and S. Morimoto: *IEEJ Trans. on IA*, **136,** 997 (2016).
3) S. Kusase and A. Shichijo: *The Papers of Joint Technical Meeting on Motor Drive and Rotating Machinery IEEJ*, MD-11-020, RM-11-041 (2011).
4) Y. Nara Y. Yoshida, and K. Tajima: *The Papers of Technical Meeting on Magnetics IEEJ*, MAG-17-003 (2017).
5) Xianxin Zeng, Li Quan, Xiaoyong Zhu, Lei Xu, and Fangjie Liu: *IEEE Trans. on AS*, **29**, 0602704 (2019).
6) Fuzhen Xing, Wenliang Zhao, and Byung-ll Kwon: *IET Electr. Power Appl.*, **13**, 573 (2019).
7) Y. Yoshida, Y. Nara, and K. Tajima: *The Papers of Technical Meeting on Rotating Machinery IEEJ*, RM-17-121 (2017).

Received Oct. 31, 2019; Revised Dec. 4, 2019; Accepted Dec. 14, 2019

Journal of the Magnetics Society of Japan

Vol. 44 No. 2 (通巻第 308号) 2020年3月 1 日発行

Vol. 44 No. 2 Published Mar. 1, 2020
by the Magnetics Society of Japan
Tokyo YWCA building Rm207, 1–8–11 Kanda surugadai, Chiyoda-ku, Tokyo 101–0062
Tel. +81–3–5281–0106 Fax. +81–3–5281–0107

Printed by JP Corporation Co., Ltd.
Sports Plaza building 401, 2–4–3, Shinkamata Ota-ku, Tokyo 144–0054
Advertising agency: Kagaku Gijutsu-sha

発行：（公社）日本磁気学会 101–0062 東京都千代田区神田駿河台 1–8–11 東京YWCA会館 207 号室
製作：ジェイピーシー 144–0054 東京都大田区新蒲田 2–4–3 スポーツプラザビル401 Tel.（03）6715–7915
広告取扱い：科学技術社 111–0052 東京都台東区柳橋 2–10–8 武田ビル 4F Tel.（03）5809–1132